uOttawa

L'Université canadienne
Canada's university

FACULTÉ DES ÉTUDES SUPÉRIEURES ET POSTDOCTORALES

uOttawa

L'Université canadienne
Canada's university

FACULTY OF GRADUATE AND POSTDOCTORAL STUDIES

Jeffrey Snoddy
AUTEUR DE LA THÈSE / AUTHOR OF THESIS

M.Sc. (Physics)
GRADE / DEGREE

Department of physics
FACULTÉ, ÉCOLE, DÉPARTEMENT / FACULTY, SCHOOL, DEPARTMENT

Study on Brillouin Scattering in Optical Fibers with Emphasis on Sensing Applications
TITRE DE LA THÈSE / TITLE OF THESIS

X. Bao
DIRECTEUR (DIRECTRICE) DE LA THÈSE / THESIS SUPERVISOR

CO-DIRECTEUR (CO-DIRECTRICE) DE LA THÈSE / THESIS CO-SUPERVISOR

EXAMINATEURS (EXAMINATRICES) DE LA THÈSE / THESIS EXAMINERS

J. Armitage

R. Bhardwaj

R. Williams

Gary W. Slater
Le Doyen de la Faculté des études supérieures et postdoctorales / Dean of the Faculty of Graduate and Postdoctoral Studies

Study on Brillouin Scattering in Optical Fibers with Emphasis on Sensing Applications

Jeffrey Snoddy

Thesis submitted to the
Faculty of Graduate and Postdoctoral Studies
In partial fulfillment of the requirements
For the MSc degree in Physics

Department of Physics
Faculty of Science
University of Ottawa

Library and Archives
Canada

Published Heritage
Branch

395 Wellington Street
Ottawa ON K1A 0N4
Canada

Bibliothèque et
Archives Canada

Direction du
Patrimoine de l'édition

395, rue Wellington
Ottawa ON K1A 0N4
Canada

Your file Votre référence
ISBN: 978-0-494-58192-6
Our file Notre référence
ISBN: 978-0-494-58192-6

NOTICE:

The author has granted a non-exclusive license allowing Library and Archives Canada to reproduce, publish, archive, preserve, conserve, communicate to the public by telecommunication or on the Internet, loan, distribute and sell theses worldwide, for commercial or non-commercial purposes, in microform, paper, electronic and/or any other formats.

The author retains copyright ownership and moral rights in this thesis. Neither the thesis nor substantial extracts from it may be printed or otherwise reproduced without the author's permission.

AVIS:

L'auteur a accordé une licence non exclusive permettant à la Bibliothèque et Archives Canada de reproduire, publier, archiver, sauvegarder, conserver, transmettre au public par télécommunication ou par l'Internet, prêter, distribuer et vendre des thèses partout dans le monde, à des fins commerciales ou autres, sur support microforme, papier, électronique et/ou autres formats.

L'auteur conserve la propriété du droit d'auteur et des droits moraux qui protège cette thèse. Ni la thèse ni des extraits substantiels de celle-ci ne doivent être imprimés ou autrement reproduits sans son autorisation.

In compliance with the Canadian Privacy Act some supporting forms may have been removed from this thesis.

While these forms may be included in the document page count, their removal does not represent any loss of content from the thesis.

Conformément à la loi canadienne sur la protection de la vie privée, quelques formulaires secondaires ont été enlevés de cette thèse.

Bien que ces formulaires aient inclus dans la pagination, il n'y aura aucun contenu manquant.

Canada

Abstract

In a distributed Brillouin sensor system, it is crucial to keep the pulse energy uniform for constant signal to noise ratio. This means that the variable DC leakage (pulse base) through the electro-optic modulator must be locked. In this thesis I examine two different methods of locking the pulse base level and look at the advantages and disadvantages of each locking method. It is found that the two locking methods, one based on a lock-in amplifier and the other using proportional-integral-derivative control, both have applications in which they excel at locking the pulse base. Also, a technique to simultaneously lock the pulse base, top, and width is developed and tested.

In the field of structural health monitoring, it is often advantageous to monitor the dynamic behaviour of a structure in real-time. The traditional distributed Brillouin sensor does not allow for this dynamic measurement due to the need to sweep the frequency difference between the two lasers and subsequent averaging of waveforms. For the first time to our knowledge, a real-time vibration sensor based on polarization-state perturbations in stimulated Brillouin scattering instead of resonant frequency mismatching monitoring of the Brillouin spectrum has been proposed. The long measurement time of traditional distributed Brillouin sensors is avoided by eliminating the frequency sweep of the pump and Stokes lasers and instead locking them at a single beat frequency corresponding to the static strain of the structure in which the fiber is embedded. This unique sensor allows measurement of vibration frequencies along a sensing fiber as shown in laboratory experiments and also the detection of impact waves from passing vehicles in field tests in which the sensor was embedded in the concrete pavement of a highway. A 20 ns pulse width with potential spatial resolution of 2 m was used over a sensing length of 300 m.

Also, studies of the Brillouin linewidth under cw pump and Stokes waves are done in order to confirm the validity of a new definition of the threshold power in Brillouin fiber amplifiers which involve both input pump and input Stokes waves – all previous threshold definitions took into account only the input pump power.

Finally, some interesting lineshape characteristics such as spectral hole burning and side-lobes on the Brillouin spectrum are observed for high power 2 ns Stokes pulses and their origins explained qualitatively. The evolution of these features with increasing pump power is investigated. The effect of laser linewidth and fiber length on these features is also considered.

Statement of Originality

This work contains no material which has been accepted for the award of any other degree or diploma in any University or other tertiary institution and, to the best of my knowledge and belief, contains no material previously published or written by another person, except where due reference has been made in the text.

I give consent to this copy of my thesis, when deposited in the University Library, being available for loan and photocopying.

SIGNED: Jeff Snoddy
DATE: June 9, 2009

Supervisor: Prof. Xiaoyi Bao

Acknowledgements

I would like to thank my supervisor, Dr. Xiaoyi Bao, for giving me the opportunity to be a part of her research team and always providing support in both research and personal matters. The completion of this thesis would have been impossible without her many insightful conversations.

Favien Ravet was a constant pillar of support in the laboratory and was always willing to go out of his way to help everyone else in the lab. I owe him a great debt of gratitude for helping me with experimental setups and helping me to understand much of the physics of Brillouin scattering.

Many of my colleagues in the fiber optics lab have contributed greatly to my work: I thank Yun Li for her help and contributions to my work on locking of the pulse base and for allowing me on several occasions to use her sensor system for experiments and measurements. I thank Ziyi Zhang for support and advice during my work on the Brillouin vibration sensor. Dr. Wenhai Li, Dr. Chunshu Zhang, and Dr. Shiquan Yang have been very supportive and helpful throughout my research, always willing to provide advice when I needed it. I would particularly like to thank Dr. Wenhai Li and Dr. Chunshu Zhang for allowing me to use their field test results in chapter 5 about the SBS vibration sensor, and Feng Wang for providing me with the results of some of his calculations regarding the Brillouin spectrum of a double Stokes pulse.

Table of Contents

1 Introduction........1

1.1 Optical Fiber Sensors........1

1.2 Optical Fibers........3

2 Brillouin Scattering........6

2.1 Mathematical Treatment of Brillouin Scattering........7

2.2 Stimulated Brillouin Scattering in Optical Fibers........12

3 Distributed Brillouin Sensor and Components........18

3.1 Description of Distributed Brillouin Sensor........18

3.2 NP Photonics Fiber Lasers........24

3.3 Frequency Locking of Fiber Lasers........26

3.4 Electro-Optic Modulator........28

3.5 Lock-in Amplifier........33

4 Locking Pulse Shape for Distributed Brillouin Sensors........35

4.1 Electro-optic Modulator in distributed Brillouin sensor........35

4.2 Lock-in Amplifier Control........37

4.3 PID Control........40

4.4 Comparison of Locking Methods........41

4.5 Simultaneous Locking of Pulse Base, Width, and Height........42

4.6 Pulse base locking impact on sensor performance........45

5 Vibration Sensor Based on Stimulated Brillouin Scattering........48

5.1 Structural health monitoring........48

5.2 Distributed Brillouin sensor suitability for vibration sensing....................49

5.3 SBS based vibration sensor setup and working principles........................51

5.4 Experimental results..55

5.5 System limitations...59

5.6 Field test results..62

5.7 Brillouin vibration sensor conclusions...65

6 Linewidth Studies of SBS...66

6.1 CW linewidth vs pump and Stokes powers..67

6.1.1 CW linewidth investigation – calibration procedures..............................69

6.1.2 CW linewidth investigation – results...70

6.1.3 CW linewidth investigation – applications...73

6.2 Spectral hole burning and side-lobes in stimulated Brillouin scattering...74

7 Conclusion..88

7.1 Thesis outcomes..88

7.2 Future work...89

References...91

Publications...96

List of Figures

1.1 Step index optical fiber....................3

2.1 Spontaneous Brillouin scattering....................10

2.2 Spontaneous scattering components....................11

2.3 SBS generator....................13

2.4 SBS amplifier....................13

3.1 Distributed Brillouin sensor system setup....................20

3.2 Brillouin spectrum produced from time-domain waveforms (20 ns pulse duration was used without polarization scrambling)....................21

3.3 Brillouin linewidth as a function of pulse duration (from Bao, 1999)....................23

3.4 Power spectrum of NP Photonics fiber lasers....................25

3.5 Frequency locking system for fiber lasers....................26

3.6 Power spectrum of unlocked fiber lasers....................27

3.7 Power spectrum of locked fiber lasers....................28

3.8 Mach-Zehnder electro-optic modulator....................29

3.9 EOM transfer curve....................32

3.10 Lock-in amplifier operation....................34

4.1 Optical pulse characteristics....................36

4.2 Locking to minimum of EOM transfer curve....................38

4.3 System diagram for lock-in amplifier method of bias locking....................38

4.4 Experimental results of lock-in amplifier method with 100 mV modulation....................39

4.5 Experimental results of lock-in amplifier method with 268 mV modulation....................39

4.6 System diagram for PID method of bias locking....................40

4.7 Experimental results of PID method....41

4.8 Simultaneous locking of pulse top and base....43

4.9 Locking of pulse base....44

4.10 Locking of pulse top....44

4.11 Locking of pulse width....44

4.12 Pulse base drift during experiments....46

4.13 (a) Map of Brillouin loss with pulse base locked. (b) Map of Brillouin loss with pulse base unlocked....47

4.14 (a) Map of Brillouin loss difference between locked and unlocked cases. (b) Averaged Brillouin loss spectra (blue = locked, red = unlocked)....47

5.1 System diagram for correlation sensor (from Hotate, 2003)....50

5.2 Results of correlation system (from Hotate, 2003)....50

5.3 Brillouin vibration sensor setup....52

5.4 (a) Static Brillouin spectrum measurement. (b) Sensing mechanism based on strain-induced Brillouin frequency shift – note the power drop measured at the unstrained Brillouin frequency ν_B....52

5.5 (a) Local birefringence change caused by force on optical fiber. (b) Sesnsing mechanism based on perturbation of the polarization states – the growth in the Stokes wave traveling from right to left is represented by the red line....54

5.6 Effect of introducing pump wave – system sensitivity increases by an order of magnitude....56

5.7 Experimental setup for vibrating cantilever....56

5.8 Experimental results for vibrating cantilever....57

5.9 (a) Power spectrum of vibrating cantilever. (b) Effect of damaging cantilever (red)....58

5.10 (a) Spatial resolution of vibration sensor. (b) Vibration response of steel cantilever....59

5.11 Experimental setup of three cantilevers....60

5.12 Reference waveforms at two different polarization states (a, b)....61

5.13 Map of change in Brillouin signal as the cantilevers are moved for two different polarization states (a, b)....61

5.14 Time-averaged Brillouin signal along sensing fiber for static strain measurement at frequency shift corresponding to 1700 $\mu\varepsilon$....63

5.15 Configuration of sensing fiber in concrete slabs of highway....63

5.16 (a) Brillouin signal due to vehicles passing over concrete slabs in lanes 1 and 3. (b) Zoom in on lane 3 for 2 seconds....64

6.1 System for measuring Brillouin linewidth....67

6.2 Brillouin linewidth vs. pump power for 10 km fiber....71

6.3 Brillouin line shape vs. pump power for 10 km fiber....71

6.4 Output Stokes power vs. input pump power for 10 km fiber....72

6.5 1% criterion applied to figure 6.4....74

6.6 Example of central dip in Brillouin spectrum....75

6.7 2 ns pulse profile....76

6.8 2 ns pulse spectrum calculated with FFT....76

6.9 Calculated Brillouin spectrum using double pulse....77

6.10 Brillouin spectrum evolution with pump power using 2 ns Stokes pulses and narrow linewidth fiber lasers....79

6.11 Central region of Brillouin spectrum evolution with pump power using 2 ns Stokes pulses and narrow linewidth fiber lasers....80

6.12 Map of Brillouin loss signal over entire fiber length for (a) 9 dBm pump and (b) 13 dBm pump....80

6.13 Brillouin spectrum evolution with pump power using 2 ns Stokes pulses and broader linewidth DFB lasers....81

6.14 Improved 2 ns pulse profile....82

6.15 2 ns pulse spectrum calculated with FFT....83

6.16 Brillouin spectrum using improved pulse generator, 2 ns Stokes pulses, DFB lasers, and 2 km fiber (a, b) or 100 m fiber (c, d)....84

6.17 Brillouin scattering of Stokes pulse....86

List of Abbreviations

BFA:	Brillouin Fiber Amplifier
BFG:	Brillouin Fiber Generator
BOTDA:	Brillouin Optical Time Domain Analyzer
BOTDR:	Brillouin Optical Time Domain Reflectometer
CW:	Continuous Wave
DBS:	Distributed Brillouin Sensor
EDFA:	Erbium Doped Fiber Amplifier
EM:	Electromagnetic
EMI:	Electromagnetic Interference
EOM:	Electro-Optic Modulator
ER:	Extinction Ratio
FBG:	Fiber Bragg Grating
FOS:	Fiber Optic Sensor
FUT:	Fiber Under Test
FWHM:	Full Width at Half Maximum
GPIB:	General Purpose Interface Bus
OTDA:	Optical Time Domain Analysis
OTDR:	Optical Time Domain Reflectometer
PID:	Proportional-Integral-Derivative
PM:	Polarization Maintaining
PMD:	Polarization Mode Dispersion
SBS:	Stimulated Brillouin Scattering

SHM:	Structural Health Monitoring
SMF:	Single Mode Fiber
SNR:	Signal to Noise Ratio
SOP:	State of Polarization
TDM:	Time Division Multiplexing
WDM:	Wavelength Division Multiplexing

Chapter 1

Introduction

1.1 Optical Fiber Sensors

Fiber optic sensors have become exceedingly common in the past decades in the field of civil engineering for structural health monitoring (SHM) of civil structures such as bridges and pipelines. A growing number of bridges across Canada are being instrumented with fiber optic sensors along with the more conventional strain gauges and thermal gauges. These monitoring systems provide detailed information on the structural behavior and health of the bridges (Tennyson, 2001). There are many other applications of fiber optic sensors as well, including chemical sensing, shape sensing, and medical uses such as endoscopic imaging, among many others. Optical fiber sensors possess some significant advantages over more traditional sensors. One key advantage is the optical fiber sensors immunity to electromagnetic interference (EMI) which allows them to be deployed in locations that were previously off-limits to conventional sensors. Other advantages are their small size, environmental ruggedness, and possibility of very high sensitivity to a large array of measurands: strain, temperature, pressure, humidity, acoustics, rotations, accelerations, vibrations, and more.

Fiber Bragg gratings (FBG) consist of a pattern of spatially varying changes of the refractive index written within the core of an optical fiber. FBGs allow for the sensing of changes in temperature and strain by monitoring the narrow bandwidth of light reflected from the grating, the wavelength of which changes as the temperature or strain changes.

Many FBGs can be written onto a single optical fiber and interrogated in either a wavelength division multiplexing scheme (WDM) or time division multiplexing (TDM).

A Fabry-Perot sensor consists of a mirror held a distance d away from the polished end face of an optical fiber. Light is injected into the fiber toward the polished end face which reflects a portion of the incident light and transmits the remainder. The transmitted light travels through the distance d, reflects from the mirror and re-enters the optical fiber where it interferes with the light which has been reflected by the polished fiber end face. The detected intensity then depends on the exact distance d between the fiber end and the mirror which is connected to the fiber in such a way that d is sensitive to strain and temperature.

Both the fiber Bragg grating and Fabry-Perot sensor are examples of point sensors which measure the temperature or strain at a single location where the sensor is placed. Point sensors have the disadvantage that if an event of interest (such as a crack developing on a structure) does not occur at the exact location at which a sensor has been placed, the event will go undetected. This disadvantage can be partially alleviated by applying many of these point sensors over the entire structure, but the cost of such a system may become too high and still leave the possibility of missing important information. In order to ensure that all events are captured, a distributed sensor is needed.

The distributed Brillouin sensor (DBS) is capable of measuring both temperature and strain in a distributed fashion over sensing lengths of up to 50 km (Bao, 1995). The physical mechanism that allows for the operation of the DBS is Brillouin scattering, the scattering of light from acoustic waves which downshifts the frequency of the scattered light by an amount that varies linearly with temperature and strain.

1.2 Optical Fibers

An optical fiber is a long, thin, cylindrical dielectric waveguide made of silica glass or polymer. The most common configuration of optical fiber, known as step index fiber, consists of a core of index n_1 surrounded by a cladding layer of lower refractive index n_2, one important characteristic of an optical fiber is the relative difference between these two indices of refraction, $\Delta = (n_1 - n_2)/n_1$. Typical values for n_1 lie between 1.44 and 1.46, while Δ is usually between 0.001 and 0.02. Another important parameter which determines the number of modes that can propagate in the fiber's core is the V number which is defined as:

$$V = k_0 a \left(n_1^2 - n_2^2\right)^{\frac{1}{2}}, \tag{1.1}$$

where a is the radius of the core, $k_0 = 2\pi/\lambda$, and λ is the wavelength of the light wave. If $V < 2.405$, the fiber will support only a single mode and is called a single-mode fiber (SMF). Single-mode fibers generally have a core measuring less than 10 μm in diameter surrounded by the cladding layer which is 125 μm in diameter.

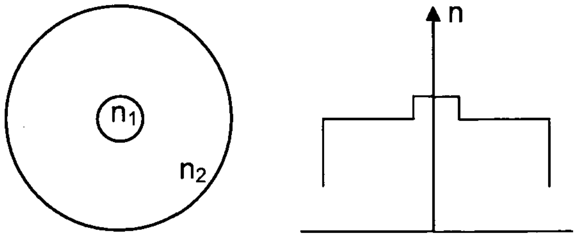

Figure 1.1 Step index optical fiber.

Even single-mode fibers support two degenerate, orthogonally polarized modes. Imperfections in the cylindrical symmetry of the fiber core or stresses in the fiber result in two orthogonally polarized modes that experience different indices of refraction, n_x and n_y. This causes a change in each mode's propagation constant, β, so that $\beta_x \neq \beta_y$ (where $\beta_x = \frac{2\pi n_x}{\lambda}$ and similar for the mode polarized in the y-direction), breaking the mode degeneracy and causing a mixing of the two polarization modes. The two modes exchange power in a periodic manner with a certain beat length:

$$L_B = \frac{2\pi}{|\beta_x - \beta_y|} = \frac{\lambda}{B_m}, \tag{1.2}$$

where B_m is called the modal birefringence and is defined as:

$$B_m = \frac{|\beta_x - \beta_y|}{k_0} = |n_x - n_y|, \tag{1.3}$$

where n_x and n_y are the refractive indices of the two orthogonally polarized modes. In most fibers, the modal birefringence changes randomly along its length – this is due to the randomly changing fluctuations in the shape of the core along the fiber. The presence of modal birefringence in a fiber can have detrimental effects on the transmission of pulses of light down the fiber. Since each polarization mode travels at a different speed, a transmitted pulse will get spread out over a long fiber – a phenomenon known as polarization-mode dispersion (PMD). Modal birefringence can also have detrimental effects on Brillouin scattering based sensors as will be discussed further in sections 3.1 and 5.5.

Special polarization-maintaining fibers (PM) are designed with a high degree of intentional birefringence built in so that the smaller, random birefringence fluctuations have very little effect on the state of polarization. These PM fibers can have elliptical cores or include stress-inducing elements in the cladding region to ensure that the fiber has a fast axis for which light polarized in that direction travels faster and a slow axis for which the polarization mode travels more slowly. If a linearly polarized lightwave is input with its polarization direction along the fast or the slow axis, the state of polarization remains constant throughout the fiber. However, if the direction of polarization does not coincide with the fast or slow axis, the direction of polarization will continuously change along the fiber with a period equal to the beat length, which can be on the order of 1 mm for PM fibers (Rashleigh, 1983).

Chapter 2

Brillouin Scattering

There are several distinct types of light scattering that can occur from local density fluctuations, thus fluctuations in the dielectric constant ε of the scattering medium. Light scattering from non-propagating density fluctuations which does not alter the wavelength of the incident beam is known as Rayleigh scattering; this type of scattering is the reason why the sky is blue. Raman scattering is caused by the interaction of incident light with the vibrational modes of the molecules in a scattering medium, causing a wavelength shift in the process. The scattering of chief interest in this thesis, Brillouin scattering, is the scattering of light from propagating pressure waves (sound waves or acoustic phonons). All three of these light scattering processes can occur as both spontaneous and stimulated scattering. Spontaneous light scattering refers to light scattering in which the optical properties of the scattering medium are unaffected by the presence of the incident light wave. On the other hand, stimulated light scattering refers to the condition in which the fluctuations causing the scattering are induced by the presence of the incident light wave.

Brillouin scattering is the inelastic process by which light waves are scattered by acoustic phonons. First described independently by Leon Brillouin in 1922 and Leonid Mandelstram in 1926, and first experimentally verified in 1930 by Gross (Gross, 1930), this effect has garnered much attention in recent years as being useful for the sensing of temperature and strain in a distributed manner over large distances.

Brillouin scattering can be thought of as scattering of a pump wave from a moving grating (acoustic phonon) which induces a doppler frequency shift in the resulting Stokes wave. The frequency shift is dependent on many factors including the velocity of sound in the scattering medium as well as the index of refraction.

2.1 Mathematical Treatment of Spontaneous Brillouin Scattering

The fluctuations in the dielectric constant which are at the root of Brillouin scattering can be expressed in terms of the thermodynamic variables density ρ and temperature T as (Boyd, 2003):

$$\Delta\varepsilon = \left(\frac{\partial\varepsilon}{\partial\rho}\right)_T \Delta\rho + \left(\frac{\partial\varepsilon}{\partial T}\right)_\rho \Delta T \tag{2.1}$$

Since the dielectric constant has a much stronger dependence on density than temperature, the second term can be dropped (Fabelinskii, 1968). Now, expressing the density fluctuations in terms of entropy s and pressure p, we can state the variations in density as (Boyd, 2003):

$$\Delta\rho = \left(\frac{\partial\rho}{\partial p}\right)_s \Delta p + \left(\frac{\partial\rho}{\partial s}\right)_p \Delta s, \tag{2.2}$$

in which the first term represents the adiabatic density fluctuations (acoustic or pressure waves) which lead to Brillouin scattering, while the second term represents the isobaric density fluctuations producing Rayleigh scattering. By combining the appropriate terms from equations (2.1) and (2.2), we find that the dielectric constant fluctuations responsible for Brillouin scattering can be expressed as:

$$\Delta\varepsilon = \left(\frac{\partial\varepsilon}{\partial\rho}\right)_T \left(\frac{\partial\rho}{\partial p}\right)_s \Delta p \tag{2.3}$$

As mentioned above, Brillouin scattering is the scattering of light from a pressure wave, the equation of motion of which can be expressed as the acoustic wave equation (Boyd, 2003):

$$\frac{\partial^2 \Delta\tilde{p}}{\partial t^2} - \Gamma'\nabla^2 \frac{\partial \Delta\tilde{p}}{\partial t} - V_A^2 \nabla^2 \Delta\tilde{p} = 0, \tag{2.4}$$

where $\tilde{p}$ is the pressure (in which the tilde ~ is used to denote that pressure is a quantity that varies rapidly in time), V_A is the velocity of sound (or acoustic velocity), and Γ' is a damping parameter which can be expressed as:

$$\Gamma' = \frac{1}{\rho}\left[\frac{4}{3}\eta_s + \eta_b + \frac{\kappa}{C_p}(\gamma - 1)\right], \tag{2.5}$$

where η_s is the shear viscosity coefficient, η_b is the bulk viscosity coefficient, κ is the thermal conductivity, and γ is the adiabatic index. In equation (2.4), the second term results in a damping of the amplitude of the pressure wave, depending on the damping parameter Γ', and the rate of change of pressure with time.

We can gain some insight into the behavior of the acoustic wave equation by assuming an acoustic wave of the form:

$$\Delta\tilde{p} = \Delta p e^{i(qz - \Omega t)} + c.c. \tag{2.6}$$

is traveling through an acoustic medium. Upon substitution of this wave into the wave equation, we get the following dispersion relationship (Boyd, 2003):

$$q^2 = \frac{\Omega^2}{V_A^2 - i\Omega\Gamma'} = \frac{\Omega^2 / V_A^2}{1 - i\Omega\Gamma' / V_A^2} \approx \frac{\Omega^2}{V_A^2}\left(1 + \frac{i\Omega\Gamma'}{V_A^2}\right), \tag{2.7}$$

which, under the assumption that $i\Omega\Gamma'/V_A^2$ is small, and upon the introduction of the phonon decay rate $\Gamma = \Gamma' q^2$ (the inverse of which is the phonon lifetime τ_p), we find the relation:

$$q \approx \frac{\Omega}{V_A} + \frac{i\Gamma}{2V_A} \tag{2.8}$$

Introducing this form for q back into the equation for the acoustic wave, we can find that the intensity of the acoustic wave varies spatially as:

$$|\Delta p(z)|^2 = |\Delta p(0)|^2 e^{-\alpha_s z}, \tag{2.9}$$

where α_s is the sound absorption coefficient given by:

$$\alpha_s = \frac{\Gamma}{V_A} \tag{2.10}$$

In order to calculate the rate at which these acoustic waves scatter light out of the incident beam, we assume an incident optical wave of the form:

$$\widetilde{E}_0(z,t) = E_0 e^{i(k \cdot r - \omega t)} + c.c, \tag{2.11}$$

and also, that the scattered optical field is subject to the driven wave equation:

$$\nabla^2 \widetilde{E} - \frac{n^2}{c^2}\frac{\partial^2 \widetilde{E}}{\partial t^2} = \frac{4\pi}{c^2}\frac{\partial^2 \widetilde{P}}{\partial t^2}, \tag{2.12}$$

where P is the polarization of the scattering medium given as $\tilde{P} = \Delta\varepsilon\tilde{E}_0/4\pi$, and substituting in the variation in dielectric constant given by equation (2.3), we get (Boyd, 2003):

$$\begin{aligned} \widetilde{P}(r,t) &= \frac{1}{4\pi}\left(\frac{\partial \varepsilon}{\partial \rho}\right)\left(\frac{\partial \rho}{\partial p}\right)_s \Delta\widetilde{p}(r,t)\widetilde{E}_0(z,t) \\ &= \frac{1}{4\pi}\gamma_e C_s \Delta\widetilde{p}(r,t)\widetilde{E}_0(z,t) \end{aligned}, \tag{2.13}$$

where γ_e is the electrostrictive constant, and C_s is the adiabatic compressibility. Taking the thermally excited pressure wave of the form:

$$\Delta\widetilde{p}(r,t) = \Delta p e^{i(q \cdot r - \Omega t)} + c.c, \tag{2.14}$$

and combining with equations (2.12) and (2.13), we determine that the scattered light is described by the equation (Boyd, 2003):

$$\nabla^2 \tilde{E} - \frac{n^2}{c^2}\frac{\partial^2 \tilde{E}}{\partial t^2} = -\frac{\gamma_e C_s}{c^2}\left[\begin{array}{l}(\omega-\Omega)^2 E_0 \Delta p * e^{i(k-q)\cdot r - i(\omega-\Omega)t} \\ +(\omega+\Omega)^2 E_0 \Delta p\, e^{i(k+q)\cdot r - i(\omega+\Omega)t} + c.c\end{array}\right] \quad (2.15)$$

The first term in the square brackets leads to a scattered wave which is downshifted in frequency known as the Stokes wave, while the second term leads to anti-Stokes scattered light which is upshifted in frequency.

The Stokes component of the scattered field has a wavevector $k_S \equiv k - q$ and a frequency of $\omega_S \equiv \omega - \Omega$ and must satisfy the dispersion relation $\omega_S = |k_S|c/n$. For scattering to take place, the frequency and wavevector of the sound wave must take on a particular value, which in a bulk material would be determined by:

$$|q| = 2|k|\sin(\theta/2), \quad (2.16)$$

where θ is the angle between the wavevectors k and k_S, and it is assumed that $|k|$ is approximately equal to $|k_S|$ since ω is much larger than Ω. Ω can now be calculated by the dispersion relation for acoustic waves ($\Omega = |q|v$) to get (Boyd, 2003):

$$\Omega = 2|k|v\sin(\theta/2) = 2n\omega\frac{v}{c}\sin(\theta/2). \quad (2.17)$$

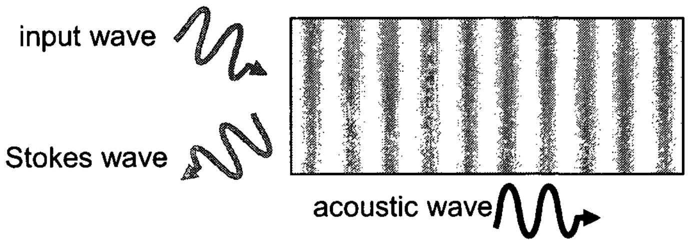

Figure 2.1 Spontaneous Brillouin scattering.

Now, it should be noted that in a single-mode fiber, the only possible directions for scattering are forward ($\theta = 0$) and backward ($\theta = \pi$), and that for forward scattering, the Stokes frequency shift is zero because the phase-matching condition amongst the three waves requires that $|q|$ be equal to zero when $\theta = 0$, this means that k_s is equal to k and that there is no frequency shift upon forward scattering. Backward scattering then is the only interesting direction in optical fibers and the resulting frequency shift is:

$$\Omega = 2n\frac{v}{c}\omega . \tag{2.18}$$

The backscattered light is not monochromatic, but has a FWHM linewidth dependent on the phonon lifetime, $\delta\omega = 1/\tau_p = \Gamma q^2$, which becomes:

$$\partial\omega = 4\Gamma'|k|^2 = 4\Gamma' n^2 \frac{\omega^2}{c^2} . \tag{2.19}$$

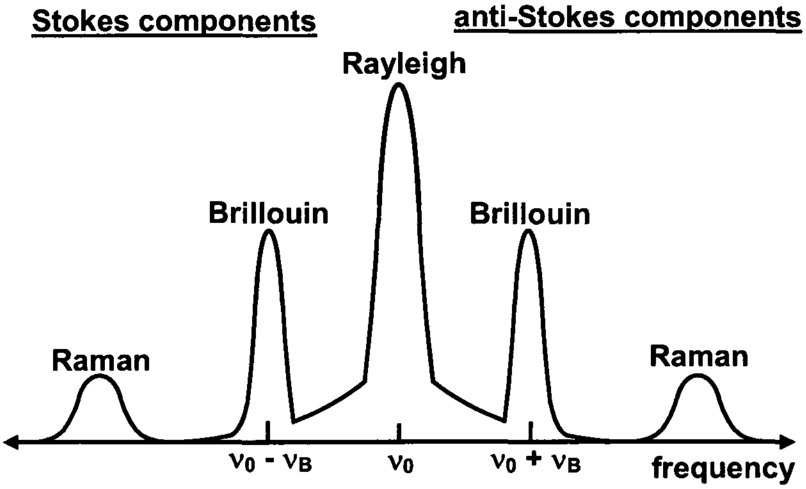

Figure 2.2 Spontaneous scattering components.

Brillouin scattering is a relatively narrow-band process with a natural linewidth of roughly 30 MHz in standard single-mode fiber in the spontaneous regime. The frequency relationships among several different scattering processes are shown in figure 2.2 (not to scale), in particular the Brillouin Stokes and anti-Stokes components are separated from the Rayleigh peak by the Brillouin frequency ν_B.

2.2 Stimulated Brillouin Scattering in Optical Fibers

The Brillouin scattering process described in the previous section is said to be a spontaneous scattering process because the fluctuations causing the scattering are a result of thermal effects. However, Brillouin scattering can also become a stimulated scattering process, that is, one in which the fluctuations causing the scattering are induced by the presence of the light wave. Stimulated Brillouin scattering (SBS) was first observed experimentally in 1964 in quartz and sapphire crystals (Chiao, 1964). SBS occurs when the injected pump power induces the creation of phonons in the fiber by the process of electrostriction, a phenomenon in which dielectric materials experience a force inward toward regions of high electric field thereby leading to an increase in density. The high electric field region is created by the beat pattern between the pump wave and the backscattered Stokes wave. Since the frequencies of the two counter-propagating waves are not identical, the beat pattern between them will not be stationary but will travel along the fiber in the same direction as the pump wave at the velocity of sound in the medium.

There are two ways for the Brillouin scattering to enter the stimulated regime: first, if the input pump wave is intense enough to give rise to a powerful spontaneously backscattered Stokes wave, the pump and Stokes will beat together to induce electrostriction in the fiber and initiate SBS; second, a Stokes wave can be input from the opposite end of the fiber which beats with the pump and causes energy from the pump to be transferred to the Stokes. The first configuration is called an SBS generator or Brillouin fiber generator (BFG) while the second is an SBS amplifier or Brillouin fiber amplifier (BFA). It should be noted that the SBS interaction only happens efficiently in the SBS amplifier if the pump and Stokes waves are separated in frequency by the Brillouin frequency shift, Ω_B, of the fiber under test (within the Brillouin linewidth).

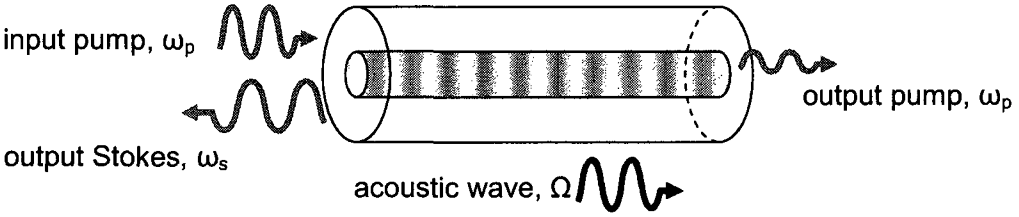

Figure 2.3 SBS generator.

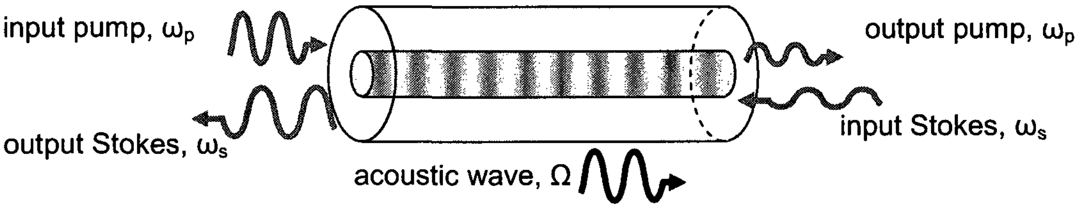

Figure 2.4 SBS amplifier

The two EM waves that interact in the SBS process (pump and Stokes) can be expressed mathematically as (Boyd, 2003):

$$\begin{aligned}\widetilde{E}_p(z,t) &= A_p(z,t)e^{i(k_p z-\omega_p t)} + c.c\\ \widetilde{E}_s(z,t) &= A_s(z,t)e^{i(-k_{sp} z-\omega_s t)} + c.c\end{aligned} \tag{2.20}$$

and the acoustic density wave is expresses as (Boyd, 2003)

$$\tilde{\rho}(z,t) = \rho_0 + \left[\rho(z,t)e^{i(qz-\Omega t)} + c.c\right], \tag{2.21}$$

where $\Omega = \omega_p - \omega_s$, $q = 2k_p$, and ρ_0 is the average density of the fiber. As before, the density is assumed to satisfy the acoustic wave equation (Boyd, 2003):

$$\frac{\partial^2 \Delta\tilde{\rho}}{\partial t^2} - \Gamma'\nabla^2 \frac{\partial \Delta\tilde{\rho}}{\partial t} - v^2\nabla^2\Delta\tilde{\rho} = \frac{\gamma_e q^2}{4\pi}\left[A_p A_s^* e^{i(qz-\Omega t)} + c.c\right], \tag{2.22}$$

where the term on the right is the divergence of the force per unit volume introduced by the electrostriction caused by the pump and Stokes waves beating together.

Introducing the acoustic wave of equation 2.21 into equation 2.22 and assuming that the acoustic amplitude varies slowly, we get (Boyd, 2003):

$$-2i\Omega\frac{\partial \rho}{\partial t} + \left(\Omega_B^2 - \Omega^2 - i\Omega\Gamma_B\right)\rho - 2iqv^2\frac{\partial \rho}{\partial z} = \frac{\gamma_e q^2}{4\pi}A_p A_s^* \tag{2.23}$$

This equation can be simplified by omitting the term containing dρ/dz because the phonons are strongly damped and do not travel very far in the fiber. Also, if steady-state conditions are assumed, the dρ/dt term can also be dropped to find that the acoustic amplitude is given by:

$$\rho(z,t) = \frac{\gamma_e q^2}{4\pi}\frac{A_p A_s^*}{\Omega_B^2 - \Omega^2 - i\Omega\Gamma_B} \tag{2.24}$$

The spatial evolution of the pump and Stokes fields are given by (Boyd, 2003):

$$\begin{aligned} \frac{\partial^2 \tilde{E}_p}{\partial z^2} - \frac{1}{(c/n)^2}\frac{\partial^2 \tilde{E}_p}{\partial t^2} &= \frac{4\pi}{c^2}\frac{\partial^2 \tilde{P}_p}{\partial t^2} \\ \frac{\partial^2 \tilde{E}_s}{\partial z^2} - \frac{1}{(c/n)^2}\frac{\partial^2 \tilde{E}_s}{\partial t^2} &= \frac{4\pi}{c^2}\frac{\partial^2 \tilde{P}_s}{\partial t^2} \end{aligned} . \tag{2.25}$$

In these wave equations, the source term on the right is the nonlinear polarization which is given by (Boyd, 2003):

$$\tilde{P} = \frac{1}{4\pi\rho_0}\gamma_e \tilde{\rho}\tilde{E}. \tag{2.26}$$

The components of this nonlinear polarization that can influence the pump and Stokes waves are the components that oscillate at the pump and Stokes frequencies, these contributions are (Boyd, 2003):

$$\begin{aligned} \tilde{P}_p &= \frac{\gamma_e}{4\pi\rho_0}\rho A_s e^{i(k_p z - \omega_p t)} + c.c. \\ \tilde{P}_s &= \frac{\gamma_e}{4\pi\rho_0}\rho^* A_p e^{i(-k_s z - \omega_s t)} + c.c. \end{aligned} . \tag{2.27}$$

Introducing these equations along with equations 2.20 into the wave equations 2.25 yields the resulting coupled wave equations describing the SBS process:

$$\begin{aligned} \frac{\partial A_p}{\partial z} + \frac{1}{c/n}\frac{\partial A_p}{\partial t} &= \frac{i\omega\gamma_e}{2nc\rho_0}\rho A_s \\ -\frac{\partial A_s}{\partial z} + \frac{1}{c/n}\frac{\partial A_s}{\partial t} &= \frac{i\omega\gamma_e}{2nc\rho_0}\rho^* A_p \end{aligned} , \tag{2.28}$$

where $\omega = \omega_p \approx \omega_s$ and ρ is given by the solution of equation 2.23. These equations have no analytical solutions but can be solved numerically.

In order to make analytical solutions possible, and to gain insight into the SBS process, we can consider steady-state conditions by dropping the time derivatives in equations 2.28 and determining ρ from equation 2.24. The equations now take the following form:

$$\begin{aligned} \frac{\partial A_p}{\partial z} &= \frac{i\omega q^2\gamma_e^2}{8\pi nc\rho_0}\frac{|A_s|^2 A_p}{\Omega_B^2 - \Omega^2 - i\Omega\Gamma_B} \\ \frac{\partial A_s}{\partial z} &= \frac{-i\omega q^2\gamma_e^2}{8\pi nc\rho_0}\frac{|A_p|^2 A_s}{\Omega_B^2 - \Omega^2 + i\Omega\Gamma_B} \end{aligned} . \tag{2.29}$$

Coupled intensity equations can be derived from these coupled amplitude equations by introducing the pump and Stokes intensities as $I_p = (nc/2\pi)A_pA_p^*$ and $I_s = (nc/2\pi)A_sA_s^*$. The coupled intensity equations are (Agrawal, 2001):

$$\begin{aligned} \frac{dI_p}{dz} &= -gI_pI_s - \alpha I_p \\ \frac{dI_s}{dz} &= -gI_pI_s + \alpha I_s \end{aligned}, \tag{2.30}$$

where the fiber loss, α, has been introduced, and g is the SBS gain factor given by (Boyd, 2003):

$$g(\Omega) = \frac{g_0(\Gamma_B/2)^2}{(\Omega - \Omega_B)^2 + (\Gamma_B/2)^2} \tag{2.31}$$

and g_0 is the gain factor at the Brillouin frequency given by (Boyd, 2003):

$$g_0 \equiv g(\Omega_B) = \frac{\gamma_e^2\omega^2}{nvc^3\rho_0\Gamma_B}. \tag{2.32}$$

If pump depletion and fiber loss are ignored (I_p = constant and $\alpha = 0$), the solution to the second of the coupled intensity equations is given by:

$$I_s(z) = I_s(L)e^{gI_p(L-z)}, \tag{2.33}$$

which reveals that the Stokes wave grows exponentially as it propagates through the fiber – a good approximation of the behaviour of the Stokes wave in low loss fibers as long as the pump power is not significantly depleted.

There are several definitions of the threshold power at which the Brillouin scattering process is called "stimulated". One commonly used definition of the threshold power in an SBS generator is the power at which the backscattered Stokes wave exiting the fiber is equal in power to the input pump wave. This definition gives a threshold power of (Smith, 1972):

$$P_{th} \approx 21 \frac{A_{eff}}{g_0 L_{eff}}, \tag{2.34}$$

where A_{eff} is the effective area of the fiber core, and $L_{eff} = (1 - e^{-\alpha L})/\alpha$ is the effective interaction length of the fiber. It is clear that this definition of the threshold power is valid only for the SBS generator configuration as it does not take in to account the possibility of an input Stokes wave. In fact, there has not been a useable definition of threshold power for the SBS amplifier configuration until very recently. Ravet (2007) has introduced just such a definition based on the power at which the Brillouin linewidth is a minimum or the power at which there is an inflection point in the backscattered vs. input power curve. Some of the data used to establish this definition was collected by the author and will be discussed in chapter 6.

Chapter 3

Distributed Brillouin Sensor and Components

3.1 Description of Distributed Brillouin Sensor

The distributed Brillouin sensor (DBS) has been developed (Horiguchi, 1989, Kurashima, 1990, Culverhouse, 1989) for measuring the strain and temperature along the entire length of a sensing fiber. The Brillouin frequency shift is a material property of the fiber which varies linearly with temperature and strain (Humphreys, 1989). The temperature dependence of the Brillouin frequency shift can be expressed as (Horiguchi, 1995):

$$\nu_B(T) = \nu_B(T_r)\left[1 + C_T\left(T - T_R\right)\right], \tag{3.1}$$

where T is the temperature of the fiber, T_R is a reference temperature, and C_T is the temperature proportionality coefficient with a typical value of $9.4 \times 10^{-3}\ K^{-1}$ for single mode fiber at a wavelength of 1320 nm, giving a temperature dependence of 1.24 MHz/°C. Similarly, the strain dependence is (Horiguchi, 1995):

$$\nu_B(\varepsilon) = \nu_B(0)\left[1 + C_\varepsilon \varepsilon\right], \tag{3.2}$$

where ε is the tensile strain and C_ε is the strain proportionality coefficient, which was found to be 4.6 for single mode fiber at 1320 nm, giving a strain dependence of 0.0607 MHz/$\mu\varepsilon$. This strain proportionality coefficient was measured for single mode fiber with GeO_2-doped core and silica cladding, however, experiments have shown that altering the types and concentrations of dopants in the core does not significantly alter the strain coefficient (Horiguchi, 1995). In order to determine the temperature or strain in the fiber it is necessary to measure the Brillouin spectrum along the length of the fiber. There are a few different methods of measuring this spectrum.

In the Brillouin gain configuration, a continuous wave (cw) Stokes wave counter-propagates with a pulsed pump wave. Throughout the sensing fiber, energy is transferred from the pump pulse to the Stokes wave via the Brillouin interaction. A high-speed photodetector is used to measure the output Stokes waveform in the time domain. Locations where there was a large interaction with the pump pulse will reveal gain in the Stokes waveform and can be correlated to a location in the fiber by optical time domain analysis (OTDA). There is a significant drawback to this technique in that the short pump pulse has very little energy compared to the cw Stokes and as energy is transferred from pump to Stokes, the pump wave can quickly become depleted.

In the Brillouin loss configuration, the roles of the pump wave and Stokes wave are reversed. The Stokes wave is now pulsed and the pump wave is cw and is the waveform detected at the output. In this configuration, the energy in the pump wave is much larger and loss to the Stokes wave will not result in significant depletion for short fiber lengths. The advantage of this technique is that much longer sensing lengths become possible, indeed Bao et al. have demonstrated sensing lengths in excess of 50 km (Bao, 1995) and commercial instruments specify a 30 km range with 1.5 m spatial resolution (Omnisens DITEST-STA).

Distributed Brillouin sensors (DBS) have been shown to provide strain accuracy of 20 $\mu\varepsilon$ and spatial resolution down to 5 m over fibers as long as 22 km (Bao, 1994), also, in a SHM application using 100 m sensing fiber, the strain accuracy was found to be +/- 10 $\mu\varepsilon$ with 50 cm spatial resolution (Bao, 2001). However, the measurement time is large due to the need to scan the beat frequency of two lasers and the need to average the resulting waveform thousands of times for the purpose of the polarization scrambling and signal to noise ratio improvement. The DBS is suitable for monitoring of structures for slowly varying effects but the slow measurement time does not allow for the detection of rapid structural changes such as vibrations.

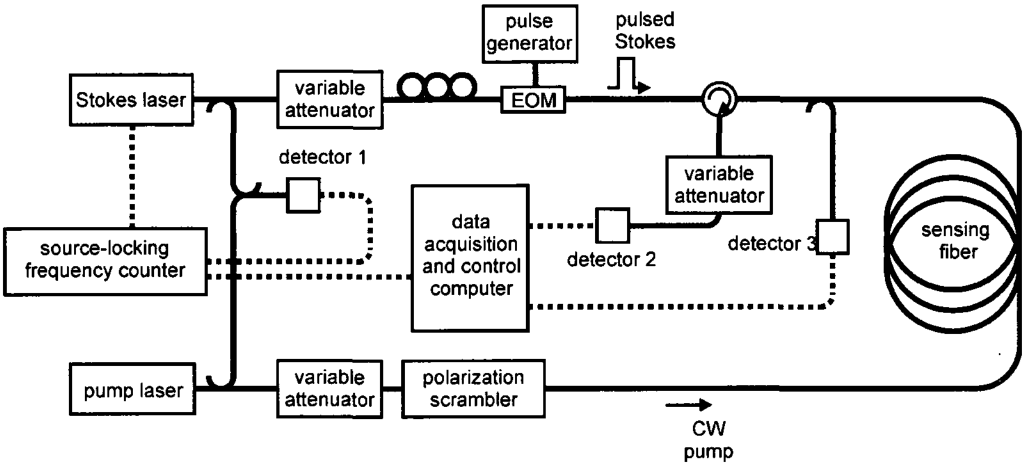

Figure 3.1 Distributed Brillouin sensor system setup.

Data collection with the DBS consists of locking the pump and Stokes lasers to a certain frequency difference (beat frequency) and collecting a time-domain waveform which corresponds to the Brillouin loss at each location in the fiber. Due to the randomly varying polarization states of the pump and Stokes waves, there will be regions inside the fiber for which the Brillouin interaction is strong (where the pump and Stokes SOP happen to be aligned), and there will be regions where there is no interaction at all, that is, where the pump and Stokes SOPs are orthogonal (Deventer, 1994). It is because of this polarization dependent sensitivity that the pump wave is put through a polarization scrambler that very quickly alters the SOP over all possible polarization states. The result of this scrambling of polarization states is that the strength of the Brillouin interaction takes on an average value throughout the sensing fiber – avoiding the occurrence of regions of zero sensitivity. After collecting the time-domain waveform at one beat frequency, the lasers are locked to a different beat frequency and another time-domain waveform is collected. This process is repeated for a range of laser beat frequencies such that the entire Brillouin spectrum is scanned. An example of several time-domain waveforms at different beat frequencies is shown in figure 3.2(a). With all of the time-domain waveforms collected, the Brillouin spectra can be obtained by displaying the data in the frequency-domain. For a given fiber location (a certain time in the time-domain waveforms), a plot of Brillouin loss vs. laser beat frequency can be produced which shows the Brillouin spectrum of the fiber at a particular location. An example of a Brillouin spectrum produced in this manner is shown in figure 3.2(b). The entire data collection can take several minutes depending on the range of frequencies scanned and the frequency spacing.

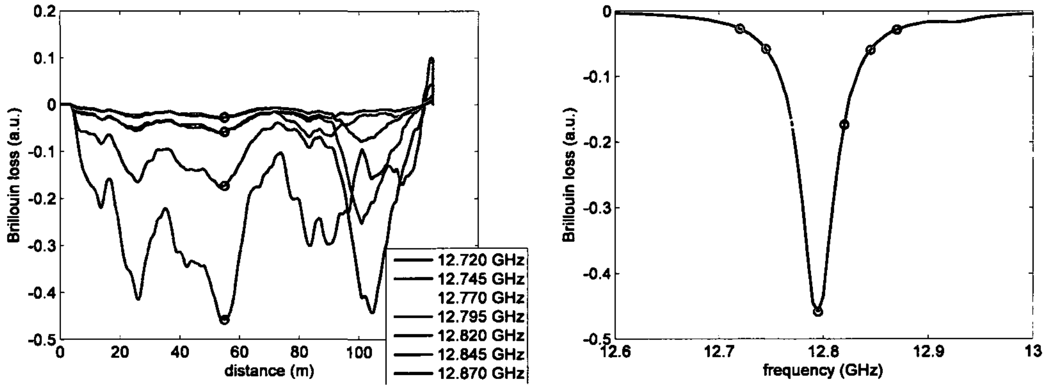

(a) (b)

Figure 3.2 Brillouin spectrum produced from time-domain waveforms (20 ns pulse duration was used without polarization scrambling).

The characteristics of the Stokes pulse have a very large impact on the performance of the DBS. The extinction ratio (Lecoeuche, 1999, and Zou, 2005) and width (Bao, 1999, Bao, 2006, and Smith, 1999) of the pulse have a direct effect on the spectral width of the detected Brillouin spectrum and thus the frequency resolution of the system and strain/temperature measurement accuracy (Horiguchi, 1995). There is a trade-off between the spatial resolution of the system and the measurement accuracy. In order to achieve high spatial resolution, the probe pulse should be as narrow as possible (spatial resolution of 1 m corresponds to a pulse duration of 10 ns), however, as the pulse duration is reduced, the resulting spectrum of the pulse broadens. Since, the measured Brillouin spectrum is a convolution of the pulse spectrum with the natural Brillouin spectrum (Smith, 1999), when a short pulse with a very broad spectrum is used, the measured Brillouin spectrum is also very broad.

One way to get around this tradeoff between spatial resolution and measurement accuracy is to take advantage of the behaviour observed by Bao et. al. (1999) that for very short pulse duration (shorter than the acoustic relaxation time of 10 ns), the Brillouin linewidth actually narrows back down to the natural Brillouin linewidth as shown in figure 3.3. This behaviour has been explained as being caused by the DC component of the probe wave that is transmitted into the fiber due to the finite extinction ratio of the electro-optic modulator (Lecoeuche, 1999, and Zou, 2005). When the acoustic wave produced by the DC base is roughly equivalent to that produced by the pulse, the measured Brillouin spectral width remains relatively narrow (due to the influence of the DC base), while high spatial resolution of the short probe pulse is retained. However, this approach can result in gain saturation and distortion of the Brillouin spectrum, particularly for long fiber lengths (on the order of kilometers) (Bao, 2006). Also, the minimum detectable Brillouin frequency shift is increased because the shift associated with the strain/temperature at a particular fiber location (pulse contribution) must overcome the component of the Brillouin spectrum from the DC leakage which represents the average Brillouin frequency shift over the entire fiber.

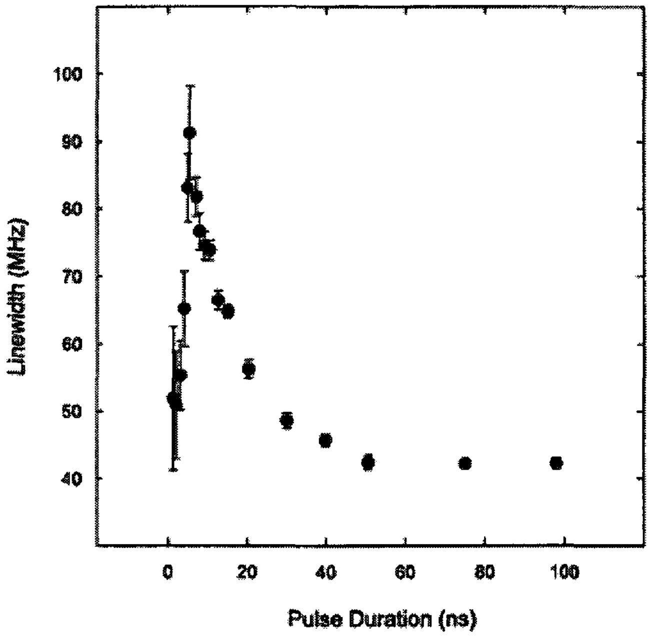

Figure 3.3 Brillouin linewidth as a function of pulse duration (from Bao, 1999).

A recently suggested method of overcoming the spatial resolution vs. measurement accuracy tradeoff is to ensure that the pump and probe lasers are phase-locked rather than merely frequency-locked (Li, 2008). In this investigation, it is suggested that the phase noise of the light sources used as pump and probe waves plays an important role in determining the width of the Brillouin spectrum with short pulses (nanoseconds). Phase-locking of the lasers generates a coherent Brillouin interaction between the pump, probe, and phonon field – producing a Brillouin linewidth which can be much narrower than the pulse spectrum. This has been experimentally verified by locking the DC pulse base to a very low level (24 dB extinction ratio), and using a short fiber length of 10 m in order to minimize the linewidth narrowing due to the contribution of the DC base. Two DFB lasers were used as the light sources with a phase-locked loop used to phase-lock their output. When phase-locking the lasers and sending probe pulses of 8.5 ns width, the Brillouin spectral width was found to be 58 MHz, much narrower than the 125 MHz expected from the pulse spectrum. Moreover, in a direct comparison of phase-locking and frequency-locking for a 2 km fiber and 10 ns pulse width, the Brillouin linewidth for phase-locking was 52 MHz, and for frequency-locking was 110 MHz (Li, 2008).

3.2 NP Photonics Fiber Lasers

The lasers used for many of these experiments were narrow linewidth fiber lasers produced by NP Photonics, the *Scorpion Benchtop Erbium Micro Fiber Laser*. These fiber lasers consists of an erbium doped optical fiber as the gain medium and two fiber Bragg gratings to form the laser cavity. A narrow bandwidth FBG is used for the laser output coupler, while the other FBG, through which the pumping energy is delivered, is much wider and more highly reflecting. The lasers have a very narrow heterodyne linewidth of <5 kHz with frequency stability of <50 MHz over one hour and provides an output power of 50 mW with power stability of ±1% (NP Photonics, 2006). The wavelength of operation is tunable from 1530 nm to 1565 nm. The frequency can be modulated in two separate ways. By adjusting the temperature of the fiber Bragg gratings, the reflected wavelength can be finely tuned over a time-scale of tens of seconds. Alternatively, fast modulation of the wavelength can be attained by piezo control of the fiber length.

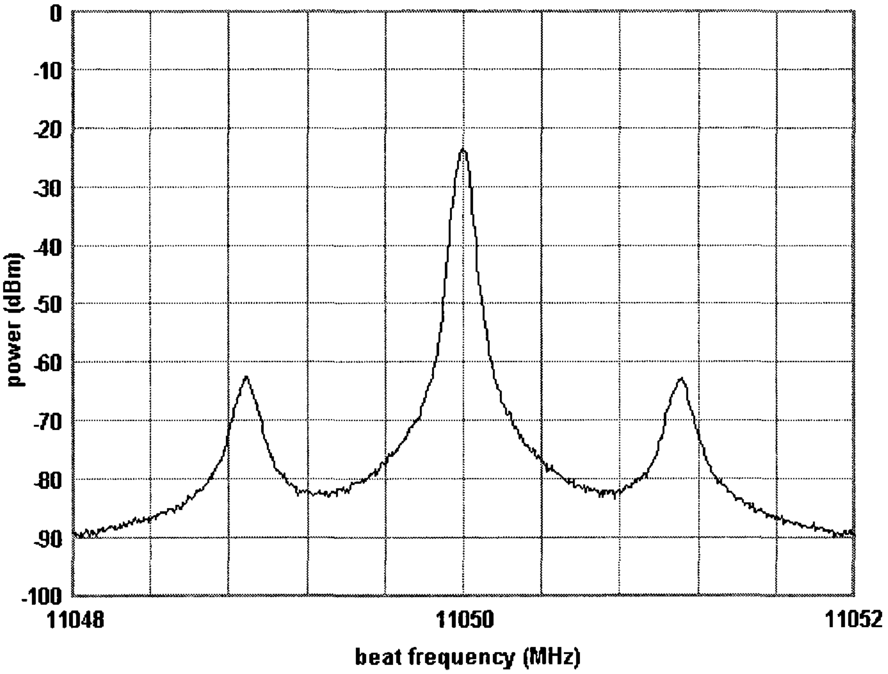

Figure 3.4 Power spectrum of NP Photonics fiber lasers.

The power spectrum of the fiber lasers was obtained by using an electrical spectrum analyzer to analyze the electrical signal output from a 12 GHz photodetector detecting the beat signal from the two fiber lasers. The resulting spectrum is shown in figure 3.4, where it is clear that there are two side peaks separated by roughly 1.1 MHz from the main peak. However, these side peaks lie 40 dB below the power of the main peak, so should not affect the performance of the Brillouin sensor.

3.3 Frequency Locking of Fiber Lasers

To take accurate measurements using the DBS, the difference in frequency between the pump and Stokes lasers must be known very accurately and must not fluctuate. In order for this to be the case, the lasers must be frequency locked.

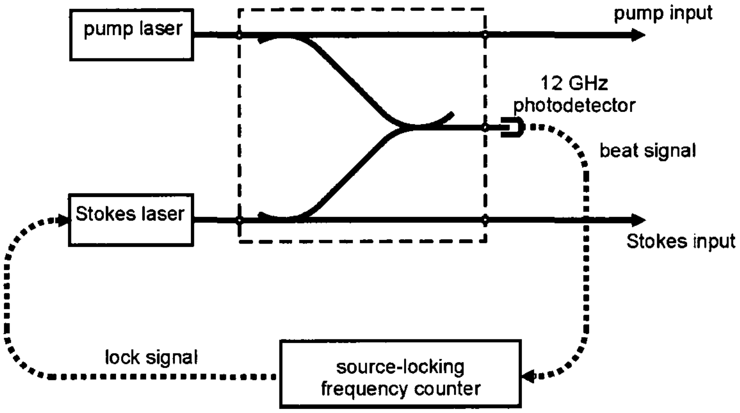

Figure 3.5 Frequency locking system for fiber lasers.

The method used to frequency lock the fiber lasers is through the use of a source locking frequency counter (XL Microwave 3201) which operates up to a frequency of 20 GHz and has a locking resolution of 1 Hz. The output from the pump and Stokes lasers is fed into a "lock box" (dashed line in figure 3.5) where a small portion of each of the two laser fields are tapped off and beat together by a 3 dB optical coupler. The beat wave is sent to a 12 GHz AC photoreceiver (New Focus model 1544) which produces an electrical beat signal to be sent to the source locking frequency counter. At the high beat frequencies for the DBS which are in the GHz range, the frequency counter down-converts the input signal to an intermediate frequency (IF) by mixing the signal with an internal signal from the local oscillator. The IF count is then added to or subtracted from a multiple of the local oscillator frequency to determine the frequency of the input signal (XL Microwave 3201 operating manual). The detected input frequency is compared to the programmed lock frequency and a lock signal is output to one of the lasers to keep it phase locked. The polarity of the lock signal is automatically determined by the frequency counter, therefore it is possible to lock the frequencies of the two lasers by sending the lock signal to either of the two lasers. Alternatively, the lock signal can be sent to an inverting splitter which then sends the lock signal to both lasers but with opposite polarity – this results in a locking range twice as large as locking with one laser alone.

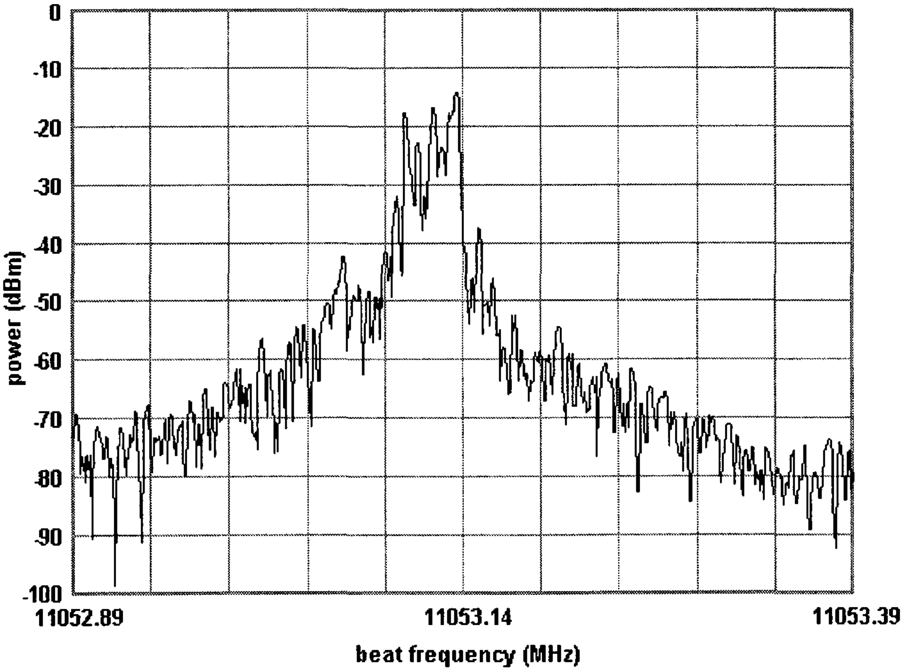

Figure 3.6 Power spectrum of unlocked fiber lasers.

When observing the spectral width of the fiber lasers while unlocked (using the same method as described earlier), the linewidth is seen to be in the 30 kHz range (see figure 3.6). However, when the laser beat frequency is being locked, the linewidth is seen to increase to the 150 kHz range as in figure 3.7. This broadening of the laser linewidth by the locking system is negligible compared to the natural Brillouin linewidth of 30 MHz.

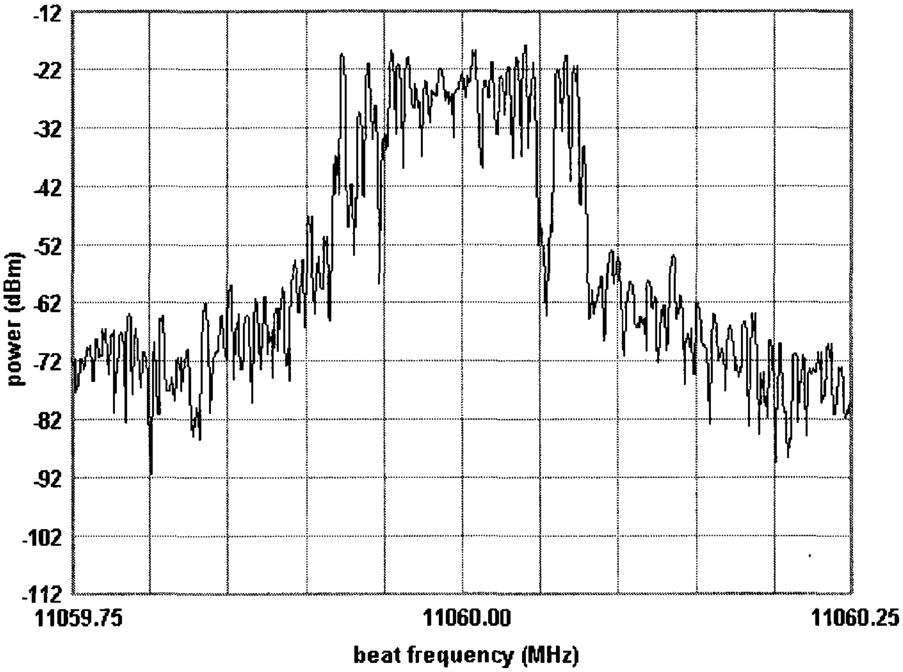

Figure 3.7 Power spectrum of locked fiber lasers.

3.4 Electro-optic Modulator

In the sensor system, a Mach-Zehnder electro-optic modulator, which operates based on the linear electro-optic effect, is used to convert a cw laser beam into a pulsed beam with controllable pulse width and extinction ratio. The Lithium Niobate ($LiNbO_3$) Mach-Zehnder EOM operates by splitting the power from the input equally at a 3 dB coupler into two "arms", at least one of which is a $LiNbO_3$ waveguide as in figure 3.8. The light waves that travel through the two arms are recombined at a second 3 dB coupler where they interfere.

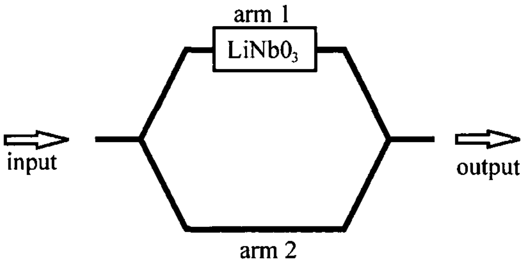

Figure 3.8 Mach-Zehnder electro-optic modulator.

Applying a voltage across the $LiNbO_3$ waveguide changes its index of refraction (through the electro-optic effect) and thus alters the speed of propagation in arm 1. When the two arms are combined back together, the optical fields will have a phase relationship, $\Delta\varphi = \varphi_1 - \varphi_2$, determined by the total voltage applied (consisting of both a bias voltage, V_{bias}, and signal voltage, V_{sig}). The amplitude of the output optical field is given by (Li, 2003):

$$A_{out} = \frac{\sqrt{2}}{2}\left(A_1 e^{i\phi_1} + A_2 e^{i\phi_2}\right), \tag{3.3}$$

where A_1 and A_2 are the amplitudes of the optical fields in each of the arms, while φ_1 and φ_2 are the phase delays upon transmission through each arm. The optical power output from the modulator is (Li, 2003):

$$P_{out} = \left|A_{out}\right|^2 = \frac{1}{2}\left[A_1^2 + A_2^2 + 2A_1A_2\cos(\phi_1 - \phi_2)\right] \tag{3.4}$$

and the transfer function of the modulator can be found by dividing this output power by the input power, $P_{in} = A_1^2 + A_2^2$:

$$T=\frac{P_{out}}{P_{in}}=\frac{1}{2}\left[1+\frac{2A_1A_2}{A_1^2+A_2^2}\cos(\phi_1-\phi_2)\right], \tag{3.5}$$

which is often simplified as:

$$T=\frac{1}{2}\left[1+b\cos(\phi_1-\phi_2)\right], \tag{3.6}$$

where

$$b=\frac{2A_1A_2}{A_1^2+A_2^2} \tag{3.7}$$

is an imbalance factor which is equal to 1 in the ideal case (equal optical power sent through each arm).

If the fields in each arm are in-phase ($\Delta\varphi = 0$) the optical output will be a maximum, while out-of-phase fields ($\Delta\varphi = \pi$) will result in minimal optical output (Li, 2003). Even when the two arms combine exactly out of phase, there will still be some intensity of light being transmitted through the modulator, this is caused by imperfections in the splitting ratios of the two 3 dB couplers (this is mathematically represented as an imbalance factor, b, which is less than 1).

$LiNbO_3$ is an electro-optic material, that is, it changes its index of refraction, and thus, output phase of any light wave traveling through it when it is subject to an applied electric field. Assuming imperfections in the manufacture of the device, there will be a phase difference between the light waves transmitted through each arm even when there is no external voltage applied, we will call this $\Delta\varphi_0$. The phase difference induced by an applied voltage, $\Delta\varphi_V$ is given by (Li, 2003):

$$\Delta\phi_V=\gamma\Delta n\frac{2\pi}{\lambda}L, \tag{3.8}$$

where γ is the optical confinement factor, Δn is the voltage-dependant change in index of refraction, and L is the length of the modulated portion of the arm. The index change can be expressed as (Li, 2003):

$$\Delta n = \frac{1}{2} n_0^3 r_{ij} \frac{V}{d}, \tag{3.9}$$

where n_0 is the index of refraction with no voltage applied, r_{ij} is the electro-optic coefficient, V is the applied voltage, and d is the distance between the electrodes. Now, the phase difference between the two arms can be expressed as:

$$\begin{aligned} \Delta\phi &= \Delta\phi_0 + \Delta\phi_V \\ &= \Delta\phi_0 + \pi\frac{V}{V_\pi} \\ &= \Delta\phi_0 + \pi\frac{V_{bias}}{V_\pi} + \pi\frac{V_{sig}}{V_\pi}, \\ &= \Delta\phi_{bias} + \pi\frac{V_{sig}}{V_\pi} \end{aligned} \tag{3.10}$$

with the parameter V_π representing the voltage at which the phase difference $\Delta\varphi_V$ is equal to π, it is given by:

$$V_\pi = \frac{\lambda d}{n_0^3 r_{ij} \gamma L}. \tag{3.11}$$

The transfer function of the Mach-Zehnder EOM can now be written in its simplest form:

$$T(V) = \frac{1}{2}\left[1 + b\cos\left(\Delta\phi_0 + \pi\frac{V}{V_\pi}\right)\right] \tag{3.12}$$

This dependence of transmittance on applied voltage is best visualized as a modulation transfer curve as in figure 3.9. The transfer curve can slowly change over time due to charging effects, or variations in temperature, wavelength, optical power, or polarization (Li, 2003, and Jungerman, 1990). The drift of the transfer function results in a drift of the optimal bias point, and the stabilization of this drift is very important to the performance of the distributed Brillouin sensor.

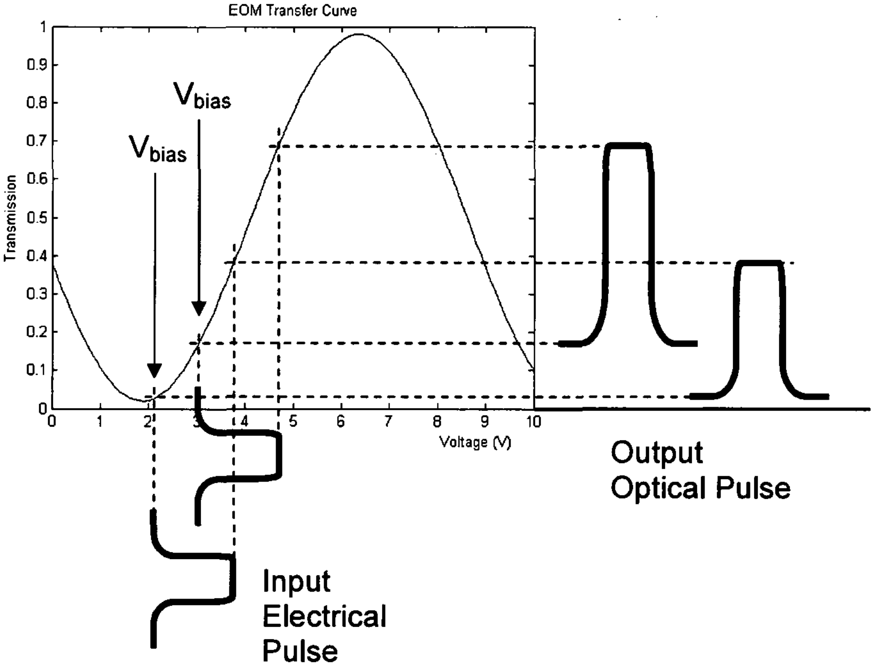

Figure 3.9 EOM transfer curve.

Figure 3.9 demonstrates the operation of the EOM in the production of optical pulses from a cw input beam. When the bias voltage is set to the minimum of the transfer curve, very little optical power is transmitted. When a voltage pulse is applied to the EOM, the total voltage (bias + pulse) climbs up the transfer curve, thereby increasing the transmission of optical power, the intensity of which depends on the magnitude of the voltage pulse. When the electrical pulse is complete, the total voltage applied to the EOM drops back down to the bias voltage, cutting off the optical transmission. The effect that drift of the bias voltage has on the transmitted optical pulses is also clearly shown. As the bias voltage drifts upward (in red), both the base of the pulse and the top of the pulse increase resulting in a dramatic drop in the extinction ratio of the optical pulse.

3.5 Lock-in Amplifier

A lock-in amplifier outputs a DC voltage that is proportional to the amplitude of the input signal at the reference frequency, and also depends on the phase difference between the input and reference (Meade, 1983).

A lock-in amplifier consists of an internal oscillator, frequency mixer, and low pass filter. It is generally used to recover signals encoded on a known carrier frequency from a noisy background. If we assume that the input and reference waveforms are both sinusoidal with the same frequency, ω, but different amplitudes (A and B respectively), and a phase difference, φ, between them, the output of the lock-in amplifier consists of a DC voltage component as well as an AC component at twice the original frequency. The DC component is dependent on the phase between the input and reference waveforms, which is why the lock-in amplifier is also called a phase sensitive detector. The AC component of the output is filtered out by a low-pass filter.

$$
\begin{aligned}
V_{in} &= A\cos(\omega t) \\
V_{ref} &= B\cos(\omega t + \phi) \\
V_{out} &= V_{in} \otimes V_{ref} \\
&= A\cos(\omega t)\cdot B\cos(\omega t + \phi) \\
&= \frac{1}{2}AB\cos\phi + \frac{1}{2}AB\cos(2\omega t + \phi)
\end{aligned}
$$

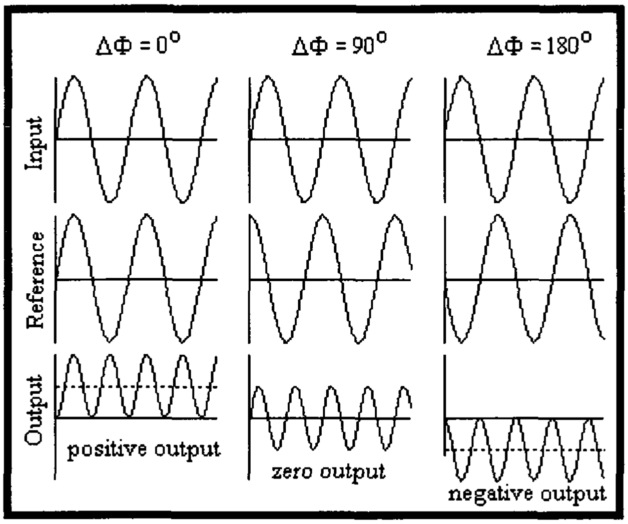

Figure 3.10 Lock-in amplifier operation.

Figure 3.10 explains the operation of the lock-in amplifier for locking applications. The input and reference waveforms will be locked to have a 90° phase shift between them. If the phase shift starts off less than 90°, the output voltage from the amplifier will be positive. This positive voltage will be applied to some part of the physics system (i.e. frequency control of a laser) which will cause the phase shift between the input and reference waveforms to increase. If the phase shift is greater than 90°, the output voltage will be negative, resulting in a decrease in the phase shift.

Chapter 4

Locking Pulse Shape for Distributed Brillouin Sensors

4.1 Electro-optic modulator in distributed Brillouin sensor

Distributed Brillouin fiber optic sensors are capable of measuring the strain and temperature along the entire length of the sensing fiber (Bao, 1995, Shahraam Afshar, 2003, Lecoeuche, 1999, and Naruse, 1999). The sensor monitors the interaction between two counter-propagating laser beams in an optical fiber, the cw pump and the pulsed probe (Bao, 1995). In order to produce the pulsed probe beam, a Mach-Zehnder electro-optic modulator (EOM) is used to turn the probe beam on and off to produce the spatial resolution for distributed sensing. It is crucial to keep the pulse energy uniform for constant signal to noise ratio. This means that the variable DC leakage (pulse base) through the electro-optic modulator must be locked. The EOM can never block 100% of the light from the laser and so the probe beam will always have a DC component in addition to the pulse (figure 4.1). The EOMs typically used in the DBS (JDS Uniphase OC-192) have a maximum extinction ratio on the order of 30 dB.

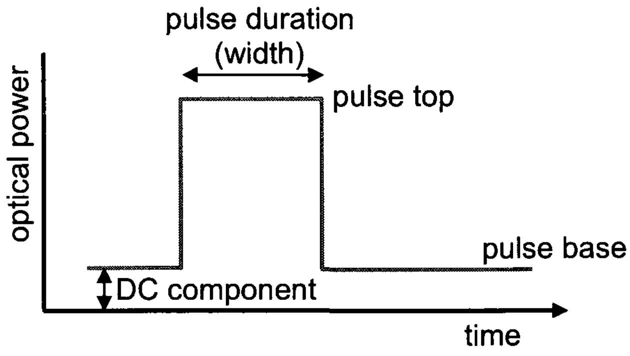

Figure 4.1 Optical pulse characteristics.

In the sensor system, the DC component is sometimes beneficial and sometimes harmful to the sensor performance depending on the application: at short pulse width (< 10 ns), some DC component is beneficial in reducing the bandwidth of the Brillouin spectrum for better measurement accuracy (Shahraam Afshar, 2003, and Lecoeuche, 1999). The critical problem with the EOM pulsing system is that, over time, the DC component does not stay constant but slowly drifts resulting in reduced sensor performance – even when a stabilized voltage is applied. This means pulse energy fluctuates with time, causing SNR variation and higher measurement error. We will look at two different methods of reducing the drift of the pulse base. The first method is to lock the pulse base using a lock-in amplifier; the second method is to lock the pulse base to a set value using a proportional-integral-derivative (PID) control algorithm implemented in software. Clearly there is a need for control of the DC level on the probe pulses and in this chapter two locking methods will be described and compared. It is found that each of the locking methods has strengths and weaknesses that make them suited to particular applications. In applications using short pulse lengths and larger DC component in short sensing fibers, the PID locking method is superior. In applications that require large extinction ratio and long fiber length, the lock-in amplifier method is the better performer.

4.2 Lock-in Amplifier Control

The lock-in amplifier can be used to lock the bias voltage to a minimum in the EOM transfer curve in the following way. The reference signal from the lock-in amplifier (Stanford Research Systems SR830) is fed into the bias port of the EOM – this provides a small modulation of f_{ref} on top of the optical pulses and ensures that the input frequency is equal to f_{ref} for optimal detection. In the case that the bias voltage is set at the transfer function minimum, the amplitude of the modulation will be very small and at a frequency of $2f_{ref}$ so that there will be zero output from the lock-in amplifier. In the case that the bias voltage has drifted away from the minimum of the transfer function, the modulation amplitude will grow larger and the phase will depend on the drift direction as described in figure 4.2. The phase of the reference signal must be set so that a positive drift of the bias voltage will provide a negative output from the lock-in amplifier and vice-versa. The drift is corrected by applying the output directly to the EOM bias port. The layout of the stabilization scheme is shown in figure 4.3. It should be noted that although the lock-in amplifier method is only capable of locking the pulse base to the minimum of the EOM transfer curve, the minimum pulse base level can be effectively increased by increasing the reference modulation amplitude. However, the increase of the pulse base level is accompanied by a significant increase in the measurement noise.

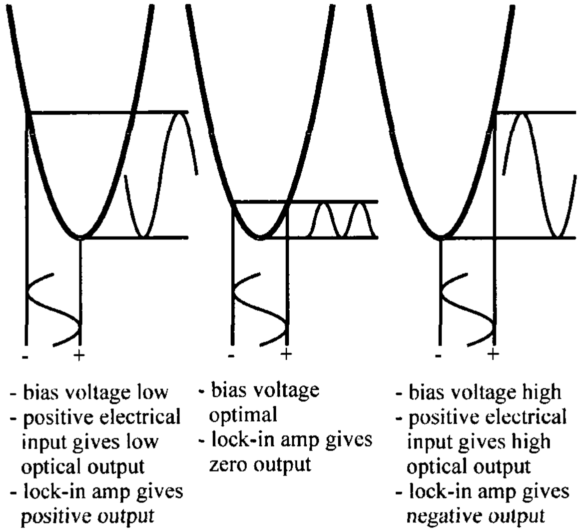

Figure 4.2 Locking to minimum of EOM transfer curve.

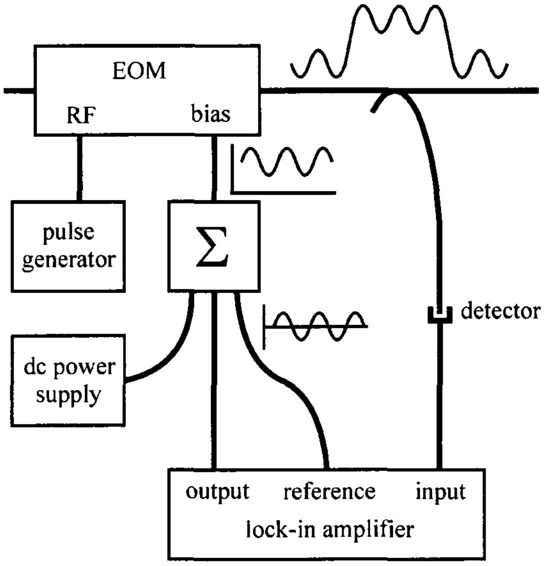

Figure 4.3 System diagram for lock-in amplifier method of bias locking.

In an experiment, it was found that the detected pulse base drifted by 1.04 μW over 11 minutes when no locking was present and drifted by only 0.47 μW over 30 minutes when locked with the lock-in amplifier using a reference modulation amplitude of 100 mV (figure 4.4). Repeating the experiment with a modulation amplitude of 268 mV yielded a pulse base drifted of 0.69 μW over 18 minutes (figure 4.5). In addition to a decrease in stability at 268 mV modulation, the rms noise in the measurement also increased from 0.14 μW to 0.49 μW.

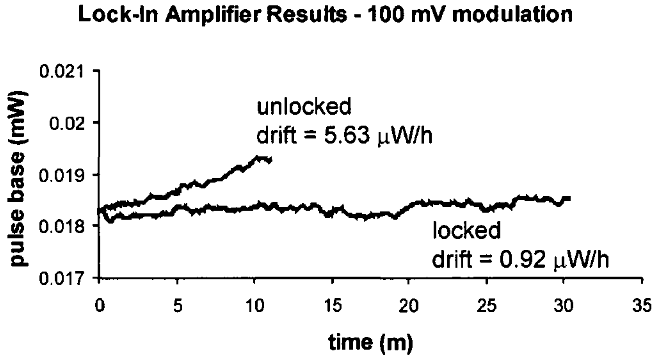

Figure 4.4 Experimental results of lock-in amplifier method with 100 mV modulation.

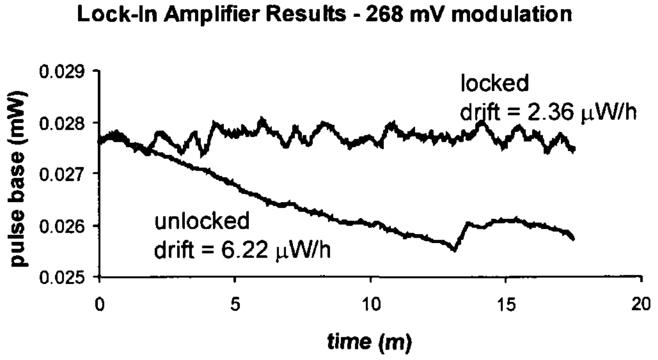

Figure 4.5 Experimental results of lock-in amplifier method with 268 mV modulation.

4.3 PID Control

PID control can be used to lock a process variable to a desired set-point (Astrom, 1995). In many cases, it is not necessary to include the derivative control, this was found to be the case in the pulse base locking scheme since the drift was a slow, gradual process. PI control alone was found to be sufficient to stabilize the bias drift. To stabilize the bias drift in the sensor system using PI control, a fraction of the Stokes beam is split off after the EOM and the pulse base is measured with a DC-coupled photodetector. The set-point of the PI controller can be chosen such that the pulse has a desired extinction ratio. The measured pulse base is compared to the setpoint to find the error signal, which is sent to the PI controller. The output from the PI controller is used to adjust the bias voltage to the EOM via a GPIB power supply. The PID locking system is shown in figure 4.6. The experimental results shown in figure 4.7 reveal that this method is successful in reducing the bias drift significantly, from 3.31 μW down to 0.36 μW over 30 minutes.

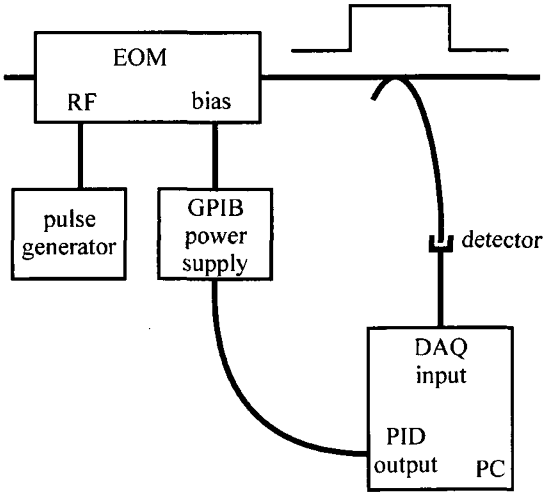

Figure 4.6 System diagram for PID method of bias locking.

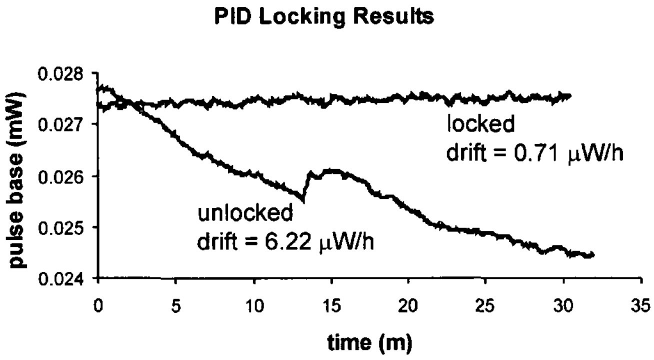

Figure 4.7 Experimental results of PID method.

4.4 Comparison of Locking Methods

The two locking methods that have been discussed have been shown experimentally to work very well in the Brillouin sensor system. However, each method has its own benefits and drawbacks and also there are applications in which only one or the other will work. In most cases, when large pulses and long fiber length are used, it is desirable to provide Stokes pulses with the largest possible extinction ratio (Shahraam Afshar, 2003, and Zou, 2005) – in this case, the lock-in amplifier method of bias locking is clearly superior. The lock-in amplifier method locks the bias voltage to the minimum of the EOM transfer curve, this is impossible to do with the PID method because it must operate on a region of the transfer curve that is monotonically increasing. There are also cases where accuracy and spatial resolution of the sensor can be increased by providing very short (1 - 10 ns) pulses with a lower extinction ratio (10 – 20 dB) (Lecoeuche, 1999, and Zou, 2005). The PID method excels in this application since the extinction ratio can be chosen arbitrarily – the lock-in method can only operate at the minimum of the transfer curve (at a set extinction ratio) and thus would not be suitable.

4.5 Simultaneous Locking of Pulse Base, Width, and Height

It is also possible to lock the pulse base, pulse top, and pulse width simultaneously using the PID method. While adjusting the bias voltage to the EOM has a roughly equivalent effect on the pulse base and pulse top levels, in order to be able to control each level independently, it is necessary to utilize a mechanism that has a greater effect on the top of the pulse than on the base. The mechanism chosen to independently control the pulse top is optical attenuation. By inserting a variable optical attenuator with GPIB communication capability (EXFO FVA-3100), the pulse base and pulse top can be controlled independently – this is because the absolute change in the power level upon attenuation variation depends on the optical power present. For example, a pulse with a peak power of 10 mW and base of 1 mW will, upon 3 dB attenuation, lose 5 mW from the pulse top but only 0.5 mW from the base.

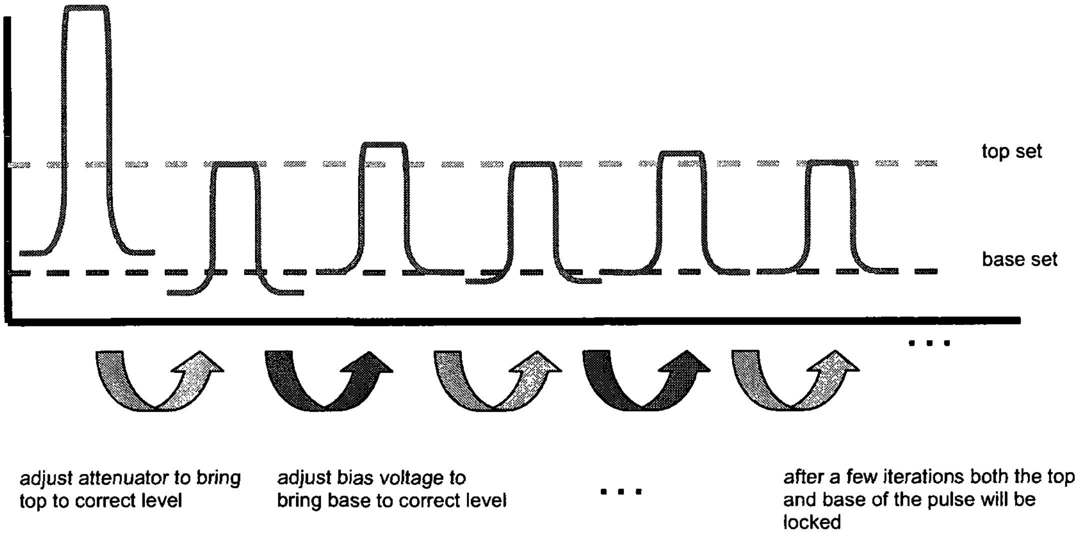

Figure 4.8 Simultaneous locking of pulse top and base.

The width of the optical pulses is set by a voltage applied to a pulse generator (Avtech AVMP-2-EW-M-N) and thus it is possible to also lock the pulse width by PID control.

Below, in figures 4.9, 4.10, and 4.11 are the results of locking the pulse base, top, and width simultaneously over a 30 minute period (blue line) in contrast with the case in which no locking was present (red line). It can be seen that locking had a great improvement in the stability of all three pulse parameters.

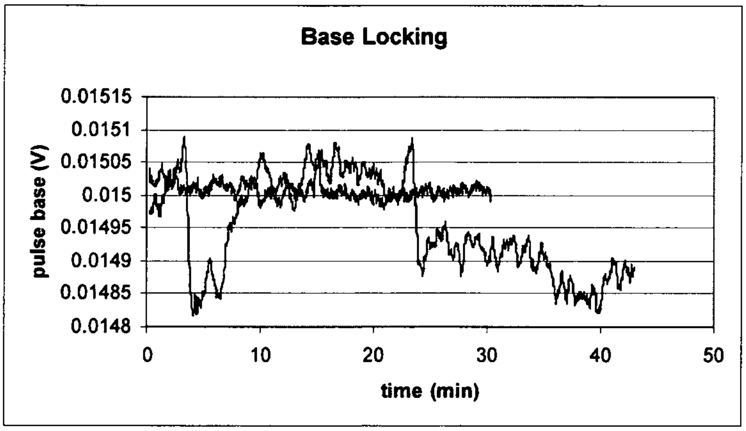

Figure 4.9 Locking of pulse base (blue = locked, red = unlocked).

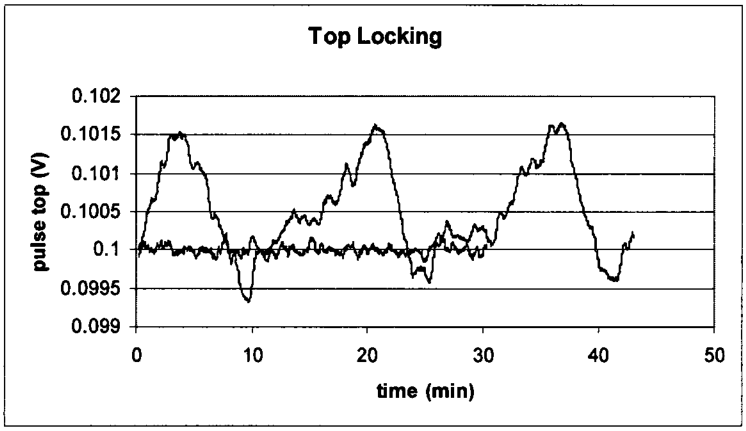

Figure 4.10 Locking of pulse top (blue = locked, red = unlocked).

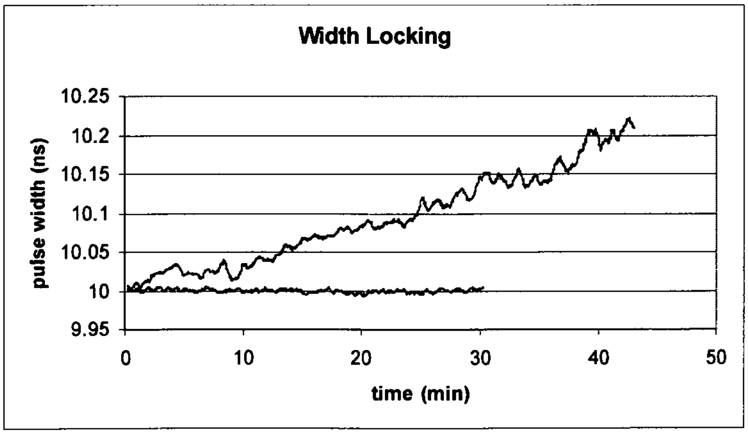

Figure 4.11 Locking of pulse width (blue = locked, red = unlocked).

4.6 Pulse base locking impact on sensor performance

All of the characteristics of the pulse (base, top, and duration) will have an impact on the performance of the distributed Brillouin sensor, in this section only the effect of the pulse base drift on sensor performance is investigated. In order to verify the improvement to sensing performance that locking the pulse base brings, an experiment was conducted with the pulse base locked and with the base unlocked. The fiber length used was 2 km and the pulse width was 10 ns. The Brillouin loss at all locations in the fiber was measured while sweeping the beat frequency of the lasers from 10.75 GHz to 11.00 GHz, the entire scan took approximately 30 minutes to complete during which time the pulse base level was also being monitored. Figure 4.12 shows the pulse base level for both runs – the blue line shows the pulse base while being locked by the lock-in amplifier method, while the red line is for the run in which the pulse base is not locked. Figure 4.13(a) shows a map of the Brillouin loss throughout the fiber in the case where the pulse base has been locked, while figure 4.13(b) shows the same information for the unlocked case – in these images, the red coloured regions correspond to the largest Brillouin loss signal while the blue regions correspond to small Brillouin loss (detuned from the Brillouin frequency shift). From these figures, it appears that turning off the locking has resulted in a slight drift of the measured Brillouin frequency toward higher frequency. Figure 4.14(a) shows a map of the difference between the Brillouin loss for the locked and unlocked cases – in this image, the yellow/red colours correspond to areas where the Brillouin loss for the locked case is larger than the unlocked case while the dark blue region is where the Brillouin loss of the unlocked case is larger. Figure 4.14(b) shows the Brillouin spectra averaged over the fiber length for both the pulse base locked (blue) and unlocked (red) cases. From these figures it can be seen that when the pulse base is not locked, it is possible for the Brillouin spectrum to become distorted as well as the detected Brillouin frequency to shift by a measurable amount, resulting in sensing errors – in this case a frequency shift of 3.28 MHz is observed corresponding to a strain error of over 50 $\mu\varepsilon$ or temperature error of over 2.5 K. Also, in this experiment it was found that the signal to noise ratio for the unlocked case was 30% lower than for the locked case. It is clear from this experiment that locking the pulse base is indeed necessary to ensure optimal sensing performance.

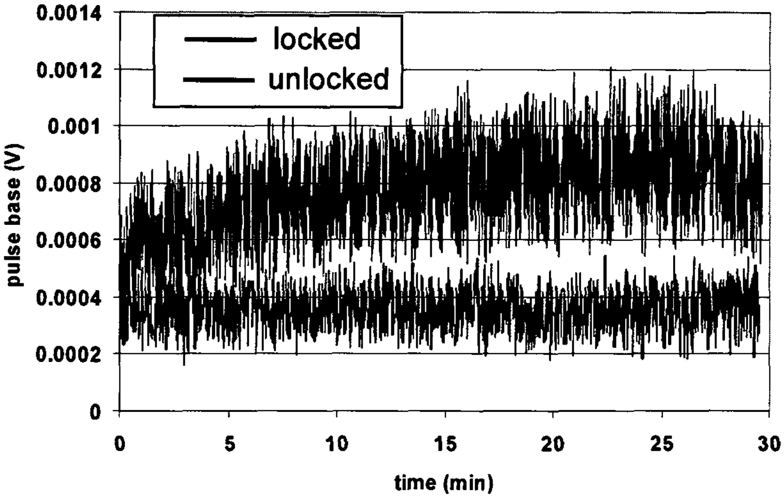

Figure 4.12 Pulse base drift during experiments.

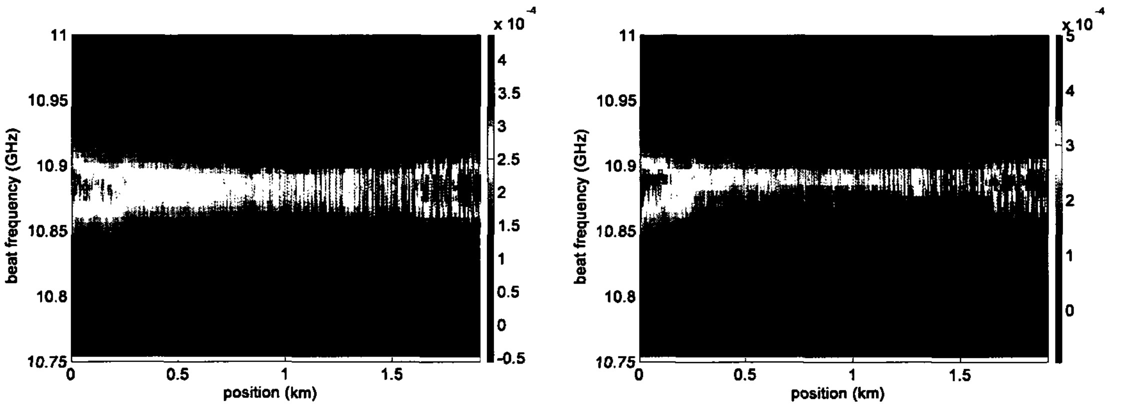

(a) (b)

Figure 4.13 (a) Map of Brillouin loss with pulse base locked. (b) Map of Brillouin loss with pulse base unlocked.

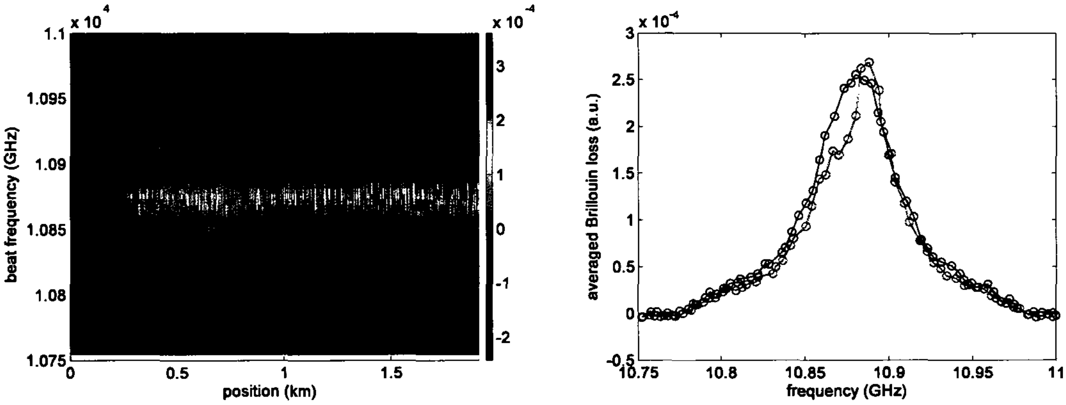

(a) (b)

Figure 4.14 (a) Map of Brillouin loss difference between locked and unlocked cases. (b) Averaged Brillouin loss spectra (blue = locked, red = unlocked).

Chapter 5

Vibration Sensor based on Stimulated Brillouin Scattering

5.1 Structural health monitoring

In recent years, the field of structural health monitoring (SHM) has been garnering much attention. The applications of SHM have expanded from civil infrastructure and aerospace transportation to ground transport, offshore and undersea structures and machinery, and biomedical devices (Chang, 2003). Monitoring of civil structures such as bridges and pipelines has become particularly important in the United States as it has been reported that 50% of all bridges were built before the 1940's and 42% are structurally deficient (Stallings, 2000).

There are many sensor technologies currently being used for SHM but they all have strengths and weaknesses. Strain gauges provide excellent accuracy and data rates but do not provide distributed information. It would require very many strain gauges to adequately cover a large structure and they still may miss important information if there is not a gauge located at the region of interest (such as a crack or buckling location for example).

Fiber Bragg grating sensors (FBGs) provide similar strengths as strain gauges with the added benefit of being immune to electromagnetic interference. While many gratings can be written into a single fiber and interrogated with wavelength division multiplexing, they are still essentially point sensors.

Distributed Brillouin sensors (DBS) can provide strain measurements in a distributed manner along long sensing fibers (many tens of km), and offer a promising application in the monitoring of civil structures.

5.2 Distributed Brillouin sensor suitability for vibration sensing

In a distributed Brillouin sensor, the Brillouin frequency (and thus temperature and strain) can be measured by sweeping the beat frequency of the pump and Stokes lasers over a range and measuring the loss of the pump wave (or gain of the Stokes wave) at each frequency to construct the Brillouin spectrum at each location in the sensing fiber. However, this need to scan the beat frequency, in addition to the need to average the resulting waveform thousands of times for the purpose of the polarization scrambling and signal to noise ratio improvement results in a very long acquisition time. A single measurement can take on the order of 10 minutes to complete, meaning that the DBS is suitable for monitoring of structures for slowly varying effects but does not allow for the detection of rapid structural changes such as vibrations, which is crucial for dynamic monitoring of structures and real time fault identification.

A few studies have been made on applying fiber optic sensors for real-time structure monitoring, one example is the correlation-based technique proposed by Hotate et al. (Hotate, 2003). This continuous wave technique provides high spatial resolution and distributed dynamic strain measurements using simulated Brillouin scattering (SBS) by simultaneously modulating the frequency of both the pump and probe waves setting up a "correlation peak" at a single location in the sensing fiber where the SBS process is excited. The system setup of this so-called Brillouin optical correlation domain analysis (BOCDA) system is shown in figure 5.1.

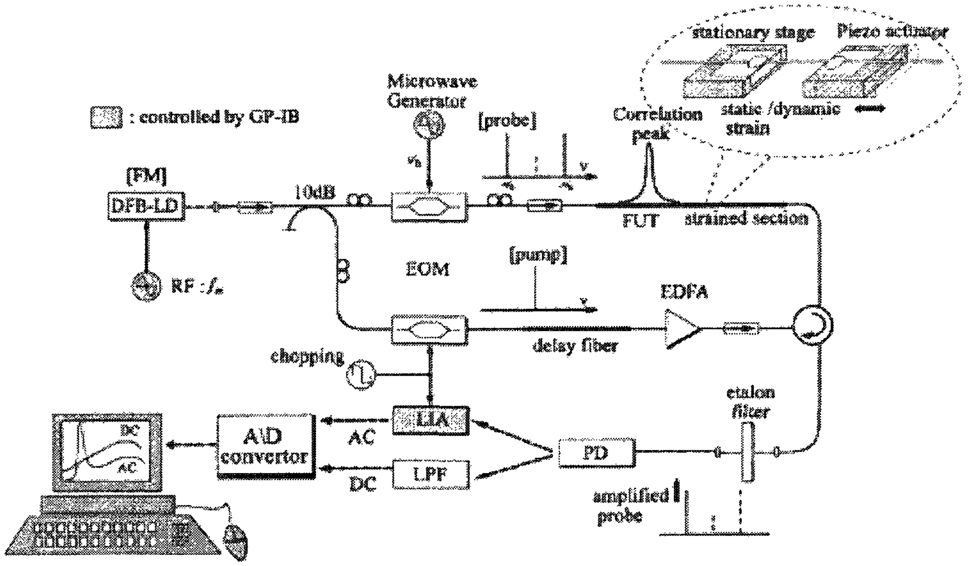

Figure 5.1 System diagram for correlation sensor (from Hotate, 2003)

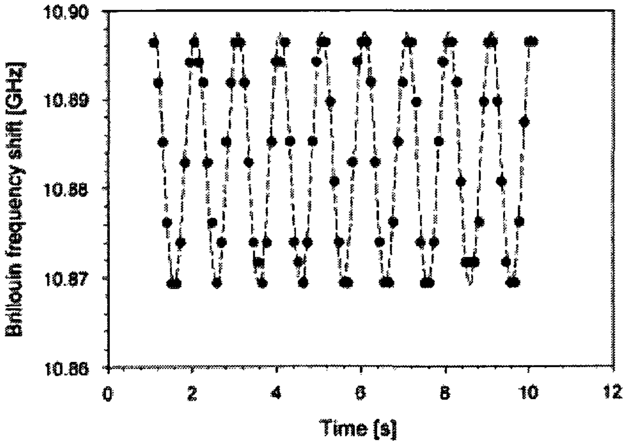

Figure 5.2 Results of correlation system (from Hotate, 2003)

The sampling rate of this system is 8.8 Hz, which gives the upper frequency response for the dynamic strain measurement. This 8.8 Hz sampling rate is for the monitoring of only a single fiber location, to get truly distributed strain information along the entire fiber length, the correlation peak needs to be swept along the fiber, resulting in a greatly reduced sampling rate which will get even worse for increased fiber lengths. It would be difficult to use this technique to monitor vibrations in civil structures such as bridges or highways because it relies on the strain as its measurement parameter which is very small in magnitude for such vibrations. Also, the fiber length used for this sensor has so far been very short in order to ensure that only one correlation peak is present in the fiber at a time - although, recent improvements to the system have demonstrated a 300 m measurement range with 20 cm spatial resolution (Song, 2006).

What is needed is a sensor system that can combine the strengths of several of these other technologies: good accuracy, high resolution, long sensing length, fast acquisition time, and the ability to measure vibrations that correspond to very small tensile strains. This chapter will describe the working principles of a real-time vibration measurement system based on SBS and provide results from a field test in which the sensor was used to detect the impact waves of passing vehicles on a section of highway.

5.3 SBS based vibration sensor setup and working principles

The vibration sensor used for initial investigations consists of counter-propagating pump and Stokes waves as shown in figure 5.3. The cw Stokes wave gets amplified by the Brillouin interaction with the pulsed pump and it is this signal that is directed to the detection arm and measured. For optimal sensitivity, the pump and Stokes laser frequencies must be locked to the Brillouin frequency corresponding to the static strain of the optical fiber under test. To determine this frequency, a simple measurement must be performed in which the beat frequency is swept and the optical output power of the Stokes wave is measured. The resulting Brillouin spectrum is shown in figure 5.4(a) - from the peak location of this figure the optimal beat frequency can be determined. Once this frequency is determined, the lasers will be locked and no further frequency sweeping will be required.

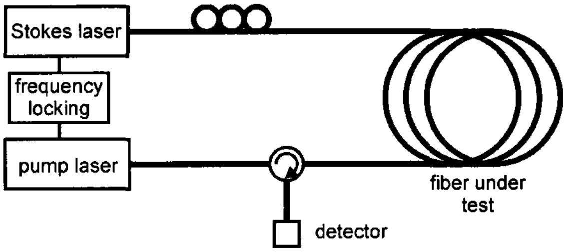

Figure 5.3 Brillouin vibration sensor setup

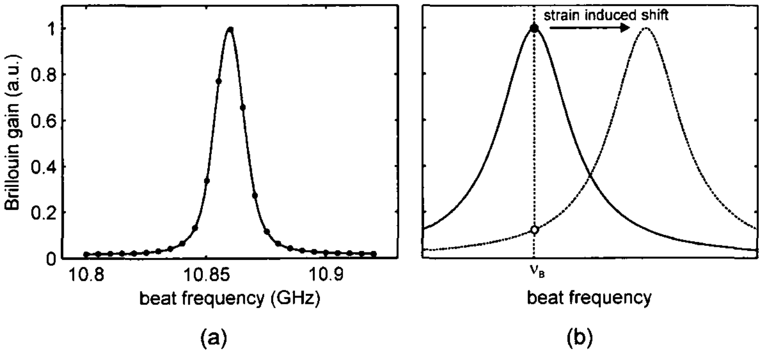

(a)

(b)

Figure 5.4 (a) Static Brillouin spectrum measurement. (b) Sensing mechanism based on strain-induced Brillouin frequency shift – note the power drop measured at the unstrained Brillouin frequency ν_B.

The main benefit of this system over traditional distributed Brillouin sensors is the increase in data acquisition rates which is made possible by locking the laser beat frequency at the Brillouin frequency of the unstrained fiber. Eliminating the need for frequency sweeping greatly reduces the time of measurement. This system is incapable, however, of measuring the Brillouin spectrum of the fiber, instead only monitoring the changes in power of the backscattered Stokes wave as the peak Brillouin frequency changes. This technique has already been used in order to monitor temperature dynamically and detect if a certain threshold temperature has been exceeded (useful for fire detection) (Ferrier, 2004, and Bao, 1996). In the fire detection system, the response time was reduced from 5-10 minutes down to 2-4 seconds. The difference between the sensor described in this paper and the dynamic temperature sensor mentioned above is that the temperature sensor does not make use of the state of polarization (SOP) of the counter-propagating waves. It has been shown that fast SOP changes are not caused by high temperature, but can be caused by large temperature gradients and dynamic stresses to the fiber by wind in Rayleigh scattering (Waddy, 2001). Therefore, for the dynamic temperature sensor, the Brillouin gain change is mainly due to the mismatching of the Brillouin frequency due to temperature rather than the changes in SOP. The main sensing mechanism of the dynamic vibration sensor is based on the local dynamic strain changes which affect the fiber birefringence and SOP at that location. The sensing mechanisms of the vibration sensor are described in more detail in the following paragraphs.

There are two physical mechanisms that make it possible to detect vibrations of an optical fiber via the effect of stimulated Brillouin scattering. One mechanism is the fact that as the fiber is undergoing vibration, there will be linear strain introduced along the fiber. The strain in the fiber will cause the Brillouin frequency of single mode fiber to shift by 0.0607 MHz/με (Horiguchi, 1995). As the Brillouin frequency shifts, the backscattered power detected will decrease as shown in figure 5.4(b). In order for the Brillouin gain to drop to half its peak value, the linear strain induced in the fiber must be approximately 300 με.

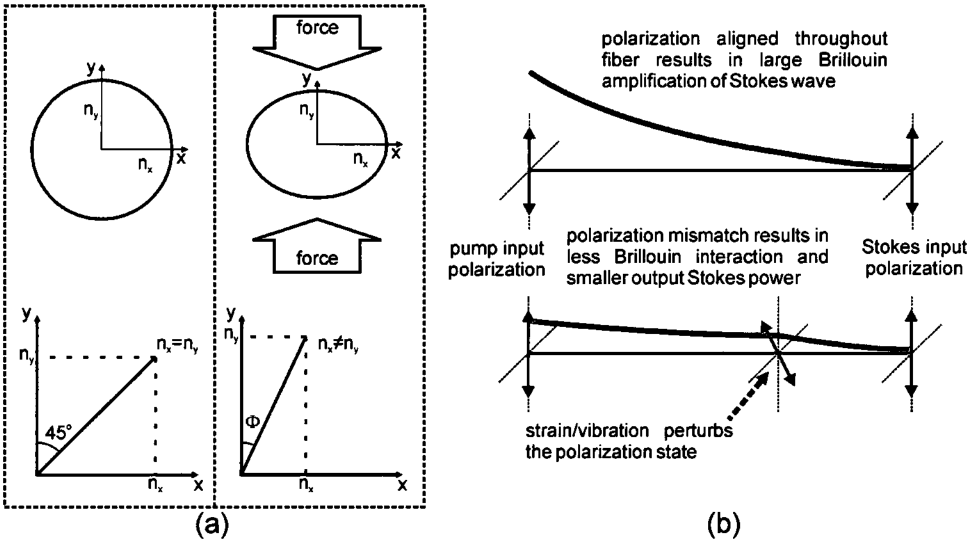

Figure 5.5 (a) Local birefringence change caused by force on optical fiber. (b) Sensing mechanism based on perturbation of the polarization states – the growth in the Stokes wave traveling from right to left is represented by the red line.

The second sensing mechanism is based on the polarization states of the pump and Stokes waves inside the sensing fiber. When an optical fiber is stretched or put under lateral pressure, the local birefringence of the fiber will be altered. This local birefringence change leads to a rotation of the local state of polarization (SOP) at an angle Φ relative to the input SOP. Here we ignore the polarization mode dispersion (PMD) for simplicity. The pump wave "sees" an SOP change of +Φ and the probe wave sees a change of –Φ. As a result, the Brillouin gain or loss will be reduced by a factor of ~cos(2Φ) in addition to the frequency mismatch term due to the strain in the fiber. This process is illustrated in figure 5.5(a).

If the pump and Stokes polarization states are aligned for an unstrained loose fiber, the Brillouin interaction will be large throughout the entire fiber (the polarization states drift only gradually). If there is a local strain effect at some location in the fiber, the polarization states will be perturbed due to a change in birefringence in the fiber causing a misalignment between the pump and Stokes polarizations (Rashleigh, 1983). The Brillouin interaction will not be optimal and the detected Stokes power exiting the fiber will be reduced as depicted in figure 5.5(b). This way, one measures the dynamic birefringence change instead of the strain change, so that the vibration frequency can be measured even when the actual strain change is very small – a definite advantage over the BOCDA technique of Hotate et. al.

Note that for the preliminary measurements of this investigation, there was no pulsing of the pump or Stokes waves and therefore, no spatial resolution was achieved.

5.4 Experimental results

For the initial experiment, the fiber under test was a 15 m length of standard single mode fiber wrapped around a piezo fiber stretcher. The PZT was supplied with a 100 Hz sinusoidal signal which stretched the fiber with amplitude of 2 $\mu\varepsilon$, which is below the strain resolution of the distributed Brillouin sensor of 10 με. In the experiment, the small strain change of 2 με is clearly detected in the form of time variation of the detected output Stokes wave. An experiment was done to determine the sensitivity increase of the system by implementing the pump wave. The results in figure 5.6 show that the sensitivity of the system was improved by an order of magnitude due to the Stokes signal amplification when the pump wave was turned on.

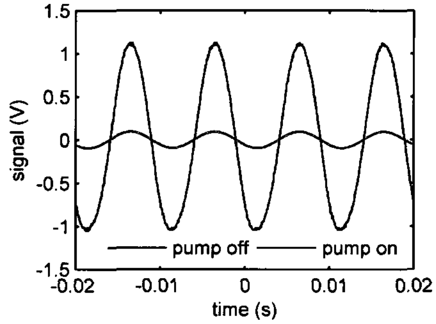

Figure 5.6 Effect of introducing pump wave – system sensitivity increases by an order of magnitude.

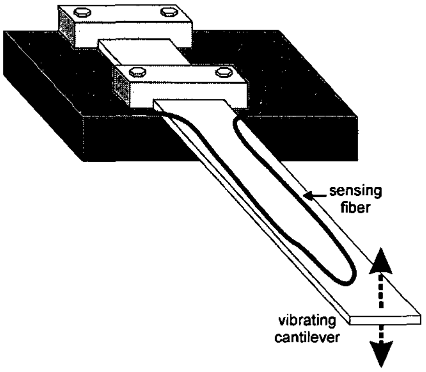

Figure 5.7 Experimental setup for vibrating cantilever.

A second experiment was done to detect the frequency of a vibrating steel cantilever. A section of fiber was bonded to the surface of a steel cantilever of which roughly 0.5 m was allowed to oscillate (figure 5.7). The oscillations of the steel strip were clearly observed as well as the damping behavior of the vibration as seen in figure 5.8. Damage to structures can be detected by changes in vibration behavior, both amplitude and frequency, and so it is imperative to measure the frequency characteristics of the vibrating structure. The Fourier transform of the data of figure 5.8 was taken and the resulting power spectrum is shown in figure 5.9(a). The main vibration frequency of 8.5 Hz is clearly evident as well as smaller contributions at other frequencies including a peak at 60 Hz which is due to electrical mains noise and should be filtered out.

To test the system's capability to measure damage to a structure, the steel cantilever was damaged and monitored. By observing the changes in the frequency spectrum, it is possible to see that the vibration characteristics of the cantilever have been modified, indicating structural damage. In figure 5.9(b), it can be seen that when damage was introduced the vibration frequencies shift lower and the secondary peak has grown significantly.

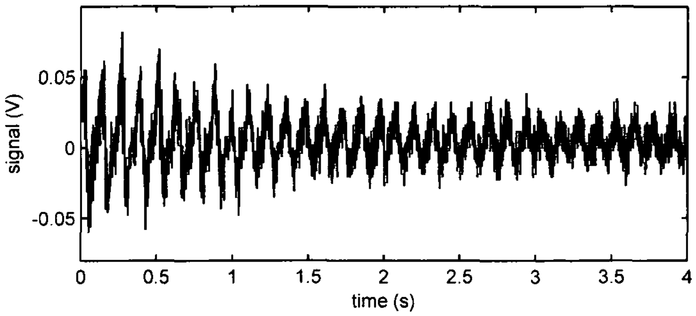

Figure 5.8 Experimental results for vibrating cantilever.

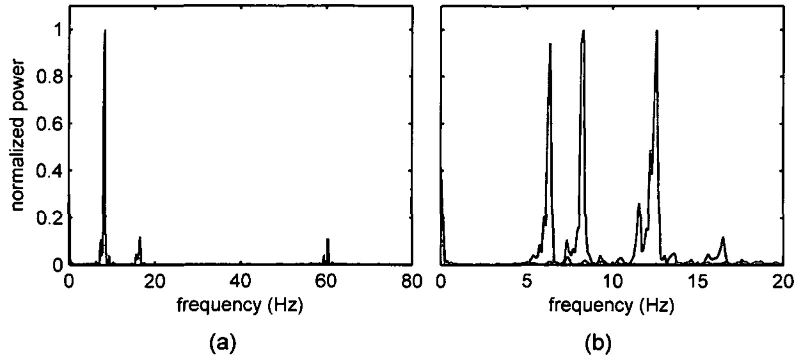

(a)

(b)

Figure 5.9 (a) Power spectrum of vibrating cantilever. (b) Effect of damaging cantilever (red).

To test the spatial resolution of the system, a $LiNbO_3$ Mach-Zehnder electro-optic modulator (EOM) was introduced to convert the cw Stokes wave into 20 ns pulses. An 80 cm section of a 120 m fiber were bonded to a 40 cm steel cantilever which was allowed to vibrate. Figures 5.10(a) and (b) shows the performance of the vibration sensor in the laboratory setting. The data shown has been processed by subtracting the waveform for the stationary cantilever to reveal only the changes in the backscattered Brillouin signal as the cantilever vibrates. The spatial resolution of the sensor is shown to be 2 m in figure 5.10(a), as expected for a 20 ns pulse. Figure 5.10(b) shows the vibration response of the steel cantilever as measured by the sensor at a sampling rate of over 100 Hz with each waveform consisting of 50 averages.

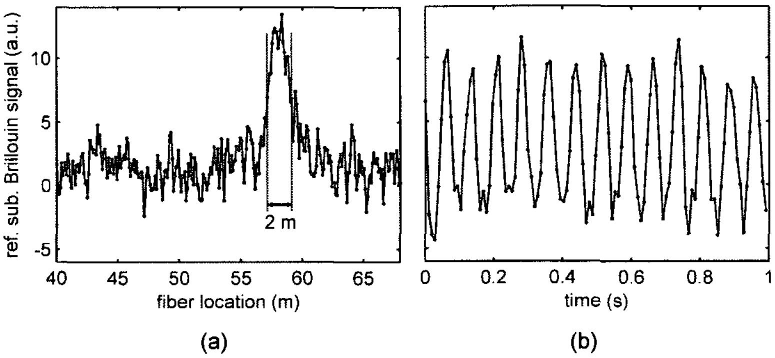

Figure 5.10 (a) Spatial resolution of vibration sensor. (b) Vibration response of steel cantilever.

5.5 System limitations

As discussed in section 1.2, the birefringence of the optical fiber varies randomly along its length - resulting in changes in the state of polarization of both the pump and Stokes waves throughout the fiber. Fortunately, this SOP pattern throughout the fiber changes only very slowly with time (on the order of several minutes) so that it does not interfere with dynamic sub-second measurements. Since the efficiency of the Brillouin interaction depends on the relative SOP of the pump and Stokes waves, these random, positional SOP changes will result in regions of low (or even zero) sensitivity along the length of the fiber along with regions of much higher sensitivity. This effect is demonstrated experimentally using a setup in which three sections of a 100 m fiber were bonded to three cantilevers of different lengths. The sections of fiber bonded to the cantilevers were separated by 5 m of fiber as shown in figure 5.11.

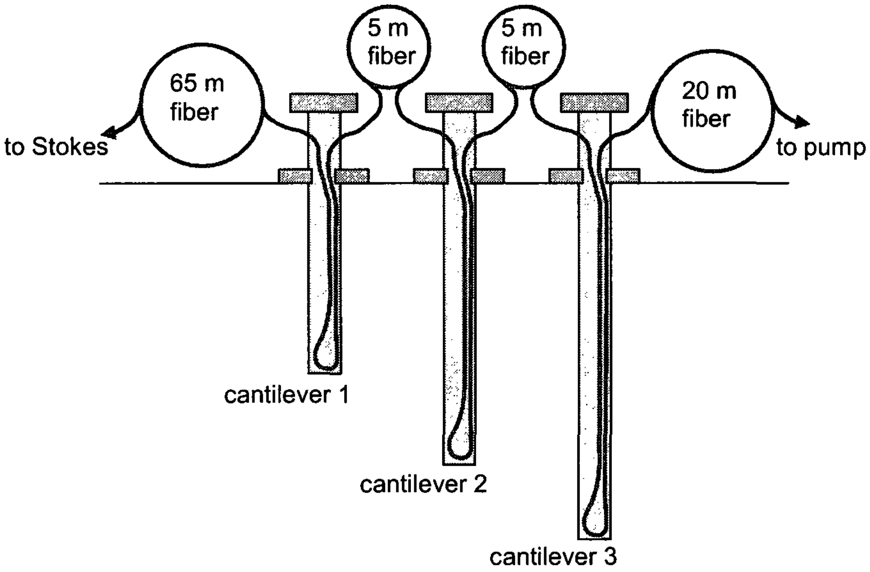

Figure 5.11 Experimental setup of three cantilevers.

In order to monitor the change in Brillouin signal as the cantilevers are moved, it is necessary to subtract a stable reference waveform from all of the waveforms which will be collected while moving the cantilevers. The reference waveforms collected at two different input pump polarization states are shown in figure 5.12 (a) and (b), the red line represents the location of cantilever 1, the green line is cantilever 2, and the blue line is cantilever 3. With the input polarizations held steady, each of the three cantilevers is bent up and down by hand while monitoring the Brillouin waveforms. The pattern of cantilever bending is cantilever 1, cantilever 2, cantilever 3, and finally, all cantilevers simultaneously. In the first trial shown in figure 5.13(a), cantilever 3 demonstrates a larger Brillouin signal change when bent than do cantilevers 1 or 2. Adjusting the input SOP of the pump wave and repeating the test results in much reduced sensitivity in cantilever 3 which now demonstrates less change in the Brillouin signal than cantilevers 1 or 2 as shown in figure 5.13(b).

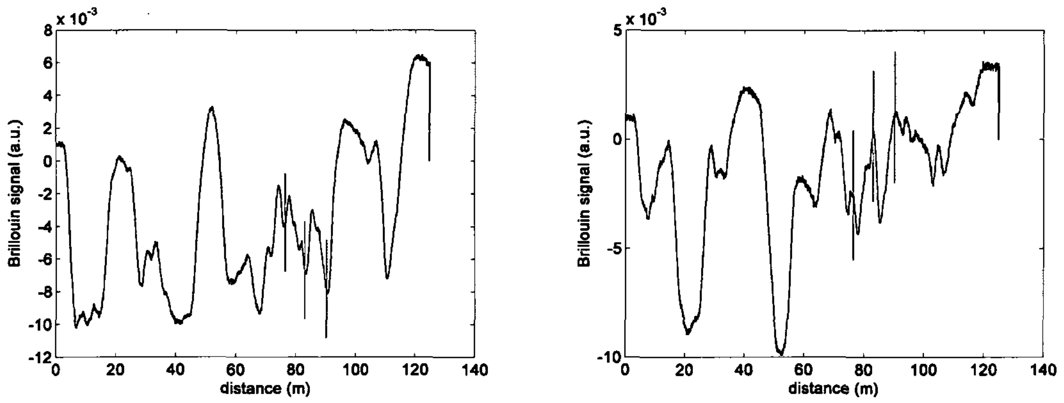

(a) (b)

Figure 5.12 Reference waveforms at two different polarization states (a, b).

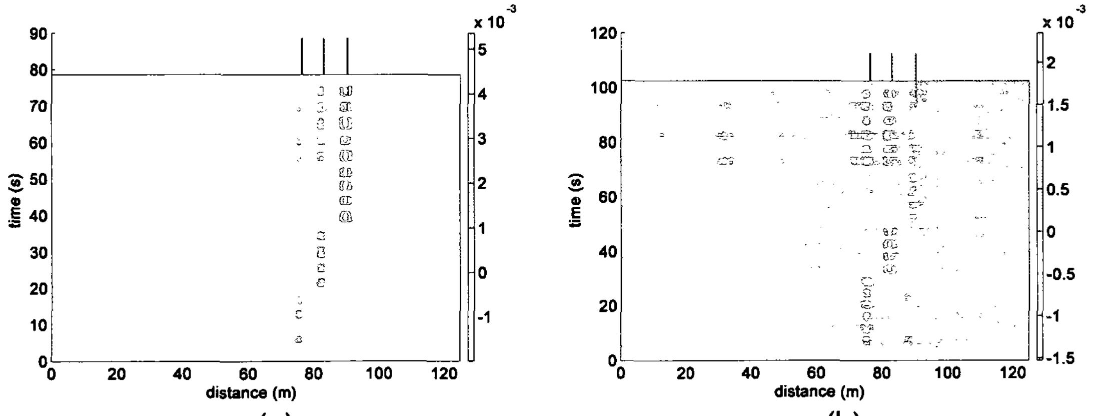

(a) (b)

Figure 5.13 Map of change in Brillouin signal as the cantilevers are moved for two different polarization states (a, b).

It is important to note that the varying sensitivity along the fiber length will affect only the amplitude of the signal being detected and has no effect on the detected frequency of vibration. The frequency of vibration at a particular location can be measured as long as the sensitivity is not zero at that location.

One possible way to minimize the effect of this limitation is to switch the input pump polarization by means of a polarization controller located just before the sensing fiber. Switching the polarization state to an orthogonal state every few seconds could ensure that all regions in the fiber have adequate sensitivity for at least one of the input polarization states.

5.6 Field test results

In order to test the feasibility of the SBS based vibration sensor in the field, my colleagues Wenhai Li and Chunshu Zhang conducted a brief field test on Highway 40, east of Montreal (the author took no part in this field test). The Brillouin sensor system used for the field test is similar to the one shown in figure 3.1, except that the polarization scrambler was deactivated for real time measurements. First, the static strain profile of the fiber embedded in the concrete pavement was measured to an accuracy of 50 $\mu\varepsilon$ with 2 m spatial resolution in the usual way to be used as the reference condition for the test. The pump and probe lasers are then locked at a frequency separation corresponding to the unstrained Brillouin frequency shift of the sensing fiber. Without the frequency scanning, the system is capable of sampling rates of 10 kHz.

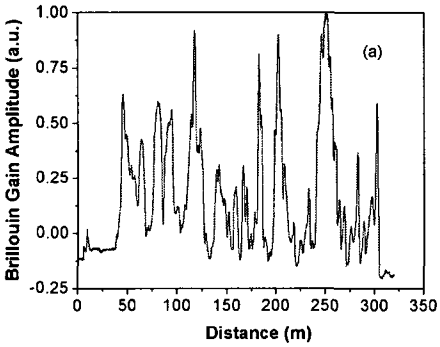

Figure 5.14 Time-averaged Brillouin signal along sensing fiber for static strain measurement at frequency shift corresponding to 1700 με.

The sensing fiber was attached to fiber reinforced polymer (FRP) bars and embedded in six full-scale continuous reinforced concrete pavement (CRCP) slabs on Highway 40 East of Montreal. The highway consists of 3 lanes which are 3.7 m wide each. The test slabs represent a 150 m long section of highway with each slab measuring 25 m long by 3.7 m wide. The sensing fiber is laid out to traverse two slabs in lane 3 (right lane) and then six slabs in lane 1 (left lane) as shown in figure 5.15.

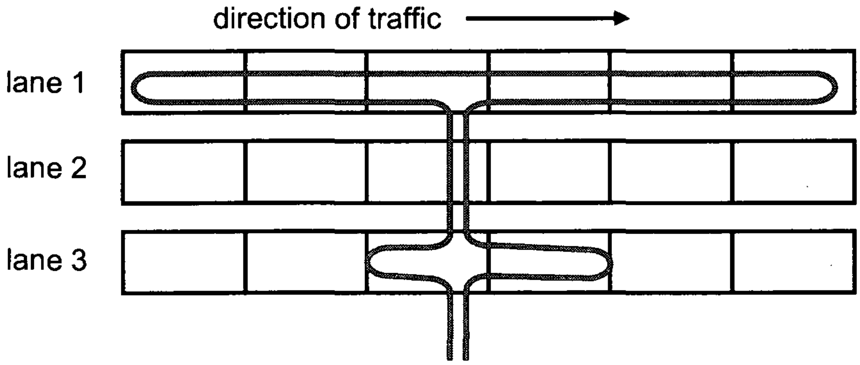

Figure 5.15 Configuration of sensing fiber in concrete slabs of highway.

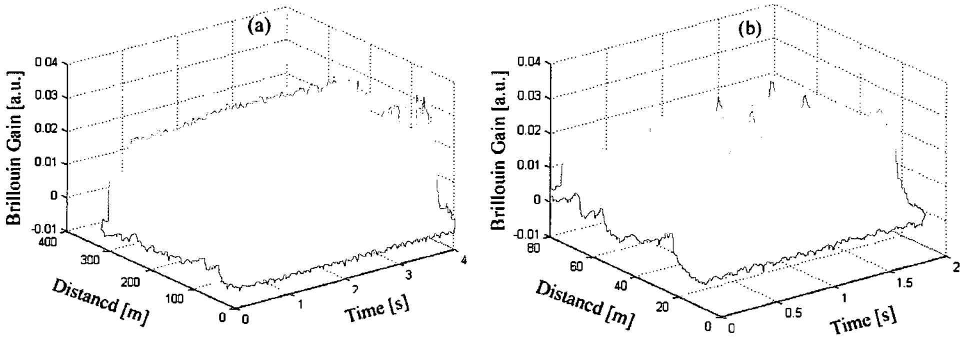

Figure 5.16 (a) Brillouin signal due to vehicles passing over concrete slabs in lanes 1 and 3. (b) zoom in on lane 3 for 2 seconds.

Dynamic data was collected with vehicles traversing the highway at high speed (>100 km/h). The sampling rate of the sensor was 10 kHz with each waveform being averaged 40 times, this means that the maximum frequency detectable was 250 Hz. Figure 5.16(a) and (b) shows the distributed impact monitoring of vehicles passing over the concrete slabs over 4 second and 2 second periods respectively. The distance between 100 m and 320 m corresponds to four slabs in lane 1 where many small cars are passing and then a large truck passes at 3.5 s. Figure 5.16(b) represents data collected from lane 3 for 2 seconds – here we see trucks (high peaks) and cars (lower peaks) passing between 0.5 - 2 s.

In general, this field test has been a good feasibility study of using the variations in the stimulated Brillouin scattering signal to detect the birefringence change in a sensing fiber by the presence of passing vehicles.

5.7 Brillouin vibration sensor conclusions

The SBS-based vibration sensor has been shown experimentally to work well for cw pump and probe waves as well as for pulsed probe to achieve spatial resolution. Laboratory tests showed spatial resolution of 2 m and sampling rate of over 100 Hz while monitoring a cantilever vibrating at 13.5 Hz. The field test using a pulsed probe wave has demonstrated impact wave detection in a distributed fashion based on polarization state changes in the sensing fiber caused by passing vehicles. The maximum sampling rate for the system is 10 kHz allowing detection of very fast events or vibrations. However, there is a tradeoff between measurement accuracy, maximum frequency response, and spatial resolution. The accuracy can be improved by increasing the number of averages and lowering the maximum frequency response.

Chapter 6

Linewidth Studies of SBS

In standard single mode fibers, the natural Brillouin linewidth is approximately 30 MHz, however, there are several factors that can affect this linewidth. In particular, when the pump power is increased, the linewidth can drop down to the 10 MHz range (Yeniay, 2002). Also, the Brillouin linewidth is affected by the linewidth of the lasers being used as well as the spectrum of the pulse. In this chapter, experiments will be discussed which probe the behavior of the Brillouin linewidth as the pump and Stokes powers are altered and the meaning this could have for introducing a definition of the Brillouin threshold.

When using SBS in a distributed temperature/strain sensor, it is necessary to pulse the input Stokes wave in order to achieve spatial resolution. The duration and shape of the pulse has a large effect on the shape and width of the frequency-domain pulse spectrum. The shape of the Brillouin spectrum can be thought of as the convolution of the natural Lorentzian spectrum with the pulse spectrum. The width of the pulse spectrum becomes significant compared to the natural linewidth in the 100 ns and lower regime and dominates below 10 ns. The pulse spectral width is not the only consideration when dealing with the Brillouin spectrum: transient effects can actually decrease the width of the Brillouin spectrum when the pulse width falls below the phonon lifetime of 10 ns (as discussed in section 3.1), while the Brillouin linewidth can broaden for pulses of longer duration due to the gain saturation and pump depletion effects for larger pulses (Smith, 1999).

6.1 CW linewidth vs pump and Stokes powers

In order to investigate the effect of input pump and Stokes powers on the Brillouin linewidth, an experiment was conducted using 10 km of single-mode fiber and cw pump and Stokes input.

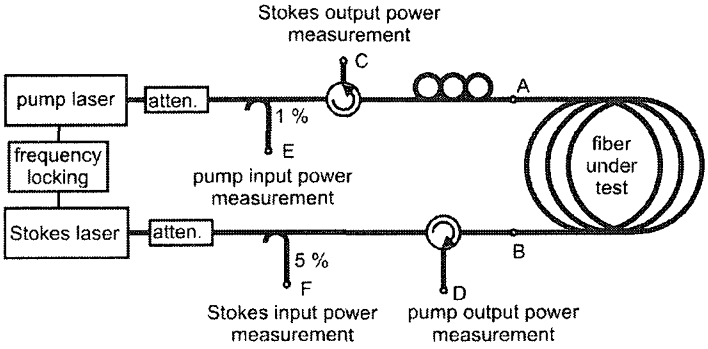

Figure 6.1 System for measuring Brillouin linewidth.

To investigate the effect of pump and Stokes powers on the linewidth and lineshape of the Brillouin spectrum, the system was set up with the configuration shown in figure 6.1. Here, the frequency difference between the pump laser and Stokes laser is locked to the Brillouin frequency shift of the fiber under test using a microwave frequency counter (XL Microwave 3201). The output from each laser is sent through a variable optical attenuator (EXFO FVA-3100) so that any desired output power can be achieved. Next, an optical coupler taps off a small amount of the power from each beam to be measured with an optical power meter to determine the input pump power and input Stokes power. After the couplers, comes an optical circulator which will allow the input light to pass through to the fiber under test while directing the output light to power meters used to determine the output pump and output Stokes powers. Finally, a polarization controller is present after the circulator in order to adjust the polarization state of the pump wave for optimal Brillouin interaction with the Stokes wave inside the fiber under test.

It can be seen from figure 6.1 that in order to measure the actual input and output powers of the fiber under test, the fiber connections would have to be broken, thereby stopping the pump and Stokes waves from counter-propagating in the fiber. Clearly, a method of determining the actual powers into and out of the fiber under test without disconnecting the fibers must be devised. This is achieved by taking power measurements at points C, D, E, and F and relating the powers measured at these points to the input and output powers of the FUT at points A and B, taking into account any optical components, connections, or losses that may appear in between. In order to achieve accurate power readings for the input pump, output pump, input Stokes, and output Stokes, it is necessary to accurately calibrate the system in the exact configuration in which it will be used to take measurements. All measurements will be calibrated with reference to the actual pump and Stokes input and output powers as measured at points A and B in figure 6.1 (the ends of the fiber under test), also, all calibrations will be made with the same power meter that will be used for future measurements. The calibrations must be completed in the proper order to avoid unnecessary disconnections/reconnections of fibers after calibrations have already been made. It is impossible to make all calibrations without subsequently making a disconnection/reconnection so it is important to ensure that the less important calibration is treated in this manner – leaving the most important calibrations until later in the calibration sequence. In this case, the most important measurements are of the pump input power and the Stokes output power. This being the case, the Stokes input power and pump output power will be calibrated first.

6.1.1 CW linewidth investigation – calibration procedures

Step one is to calibrate the Stokes input power by disconnecting the fiber at point B and place the fiber carrying the Stokes wave into a power meter (EXFO FOT-90A through channel 2 of JDS Uniphase SB Series Fiber Optic Switch). Three measurements of the Stokes input power are made at different power levels (three different attenuation levels of the variable optical attenuator) and recorded. Next, the power meter is moved to point F (where future measurements of Stokes input power will be made) and the power is measured and recorded for the same attenuation levels used previously.

The pump output power is then calibrated by connecting a power meter (EXFO FOT-90A through channel 1 of optical switch) to point B to measure the pump power output from the fiber under test at three different attenuation levels. The power meter is then moved to point D to measure the output pump output power in the location where all future measurements of the pump output will be made. At this point in the calibration sequence, the two fiber ends at point B are connected, not to be disconnected for the duration of the calibrations and measurements.

The pump input power is calibrated by disconnecting the fiber at point A and connecting a power meter (Anritsu ML 910B channel 1 with MA 9305B sensor head) to the fiber carrying the pump wave. Power measurements are made at three different attenuation levels and then the power meter is moved to point E to measure the pump power at the same three attenuation levels.

Finally, the Stokes output power is calibrated by connecting channel 2 of the Anritsu power meter to the fiber under test at point A and taking three power measurements. The power meter is moved to point C while the two fibers at point A are connected and left for the remainder of calibrations and measurements. Upon measurement of the power at point C for three Stokes attenuation levels, the collection of calibration data is complete.

6.1.2 CW linewidth investigation – results

With calibration complete, the Brillouin linewidth is determined by setting the desired pump and Stokes input powers and measuring the output Stokes power at each distinct beat frequency. The pump and Stokes frequencies were phase-locked using a source-locking frequency counter. The experimental results were fit to a pseudo-Voigt function which allows peak fitting of functions that are Lorentzian, Gaussian, or an intermediary between the two. The pseudo-Voigt function used took the form:

$$G(\nu) = G_0 + a\left[c\frac{2}{\pi b}\frac{1}{1+4\left(\frac{\nu-\nu_0}{b}\right)^2} + (1-c)\frac{2\sqrt{\ln 2}}{\sqrt{\pi}b}\exp\left(-4\ln 2\left(\frac{\nu-\nu_0}{b}\right)^2\right)\right], \qquad (6.1)$$

where G_0 is the fit parameter representing the background gain of the Stokes wave, a is the fit parameter representing the amplitude of the peak, ν_0 is the fit parameter for the central wavelength, b is the fit parameter for the linewidth (FWHM), and c is the lineshape parameter with c=1 giving a Lorentzian lineshape and c=0 giving Gaussian.

Figure 6.2 shows the experimental results of the linewidth vs. pump power experiment for a fiber length of 10 km. Note that for very small input pump power the measured Brillouin linewidth is very close to the natural Brillouin linewidth of 30 MHz. As the pump power is increased, the linewidth decreases and reaches a minimum, at a pump power and linewidth which depends on the power of the input Stokes wave. It is this power dependence of the minimum Brillouin linewidth that can be used as a threshold definition for Brillouin Fiber Amplifiers (BFA).

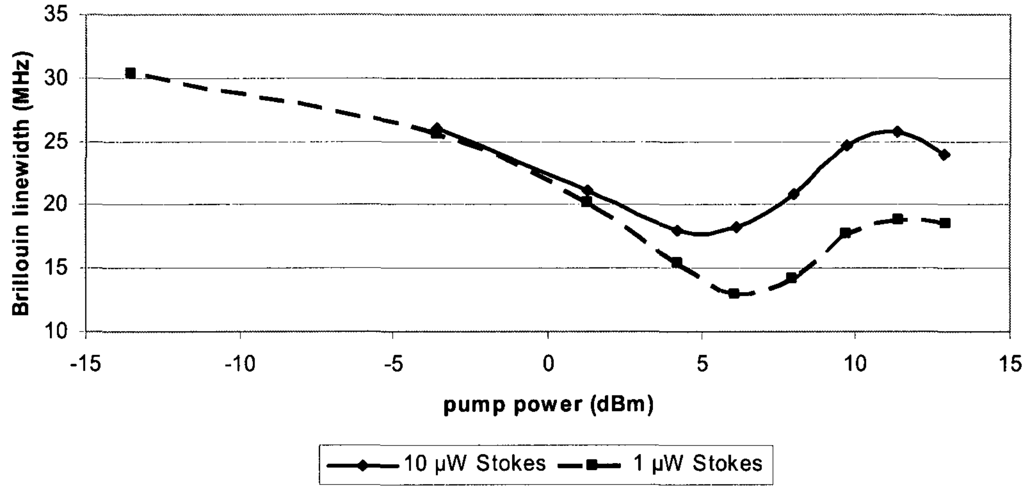

Figure 6.2 Brillouin linewidth vs. pump power for 10 km fiber.

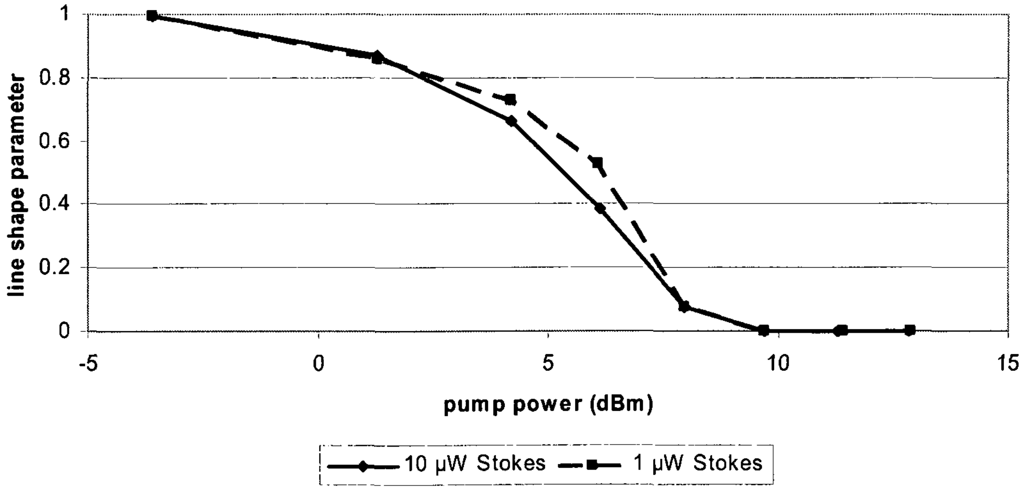

Figure 6.3 Brillouin line shape vs. pump power for 10 km fiber.

Figure 6.3 shows the evolution of the line shape of the measured Brillouin spectrum from low pump power to high pump power. The information being plotted is the c parameter from the pseudo-Voigt fit function which represents the shape of the Brillouin spectrum. As expected, at low pump power the Brillouin spectrum was Lorentzian in shape (c = 1) and gradually became more and more Gaussian as the pump power was increased.

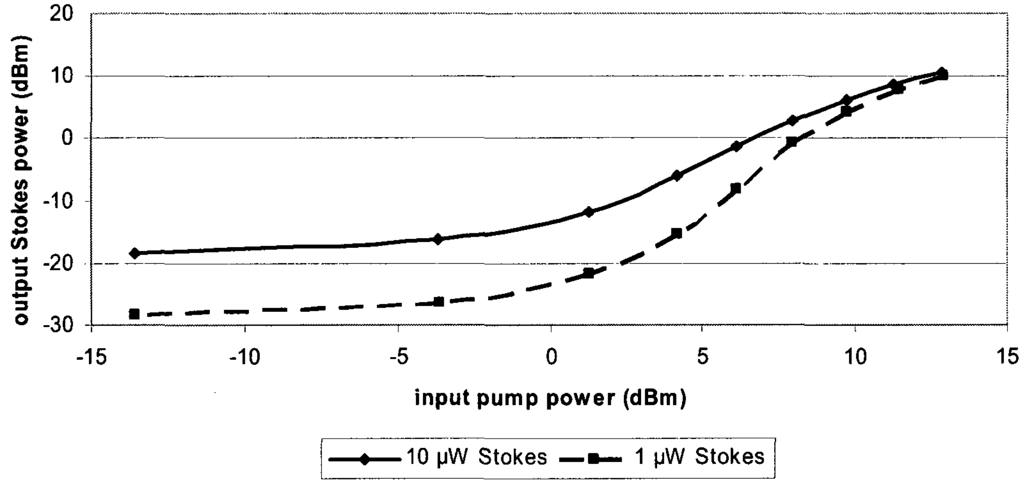

Figure 6.4 Output Stokes power vs. input pump power for 10 km fiber.

Figure 6.4 shows how the output Stokes power changes with increasing pump power input into the fiber. For these measurements, the beat frequency of the pump and Stokes lasers was held at the Brillouin frequency of the fiber under test.

6.1.3 CW linewidth investigation – applications

This experimental procedure can be used to determine the threshold power at which pump depletion begins to become significant causing a decrease in sensor performance. The traditional definition of the threshold power is given by (Smith, 1972):

$$P_{th} \approx 21\frac{A_{eff}}{g_0 L_{eff}}, \qquad (6.2)$$

However, there are problems with this definition. It is based on the definition that the threshold power is the input power for which the backscattered Stokes power is equal to the input pump power at z = 0 – an unphysical definition which neglects fiber losses. Also, this definition only applies to Brillouin fiber generator (BFG), as it does not take into account any possible input Stokes power such as is the case in a distributed Brillouin sensor. An alternative threshold definition known as the 1% criterion (Bayvel, 1990) is often used to experimentally determine the threshold power. The 1% criterion states that the threshold power is the power at which the backscattered power is equal to 1% of the input pump power. It has been pointed out by Ravet (2007) that when plotted on a logarithmic scale, the point of inflection on the plot of backscattered power vs. input pump power is very close to where the 1% criterion line intersects the curve. Also, in a Brillouin fiber amplifier the minimum linewidth corresponds very closely to this same power level.

When using the 1% criterion for the BFA configuration, it is clear from figure 6.5 that problems can arise. In this case, the 1% criterion line does not even intersect the curve representing a Stokes input power of 10 μW (so there is no threshold power given by the 1% criterion in this case), while it intersects the 1 μW Stokes input power curve twice (giving two different threshold powers). The 1% criterion clearly cannot be used for the BFA configuration.

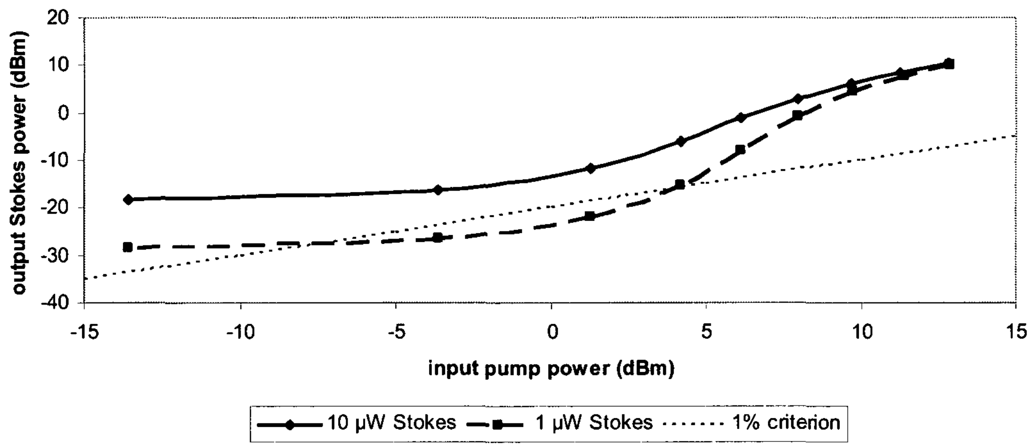

Figure 6.5 1% criterion applied to figure 6.4.

It is clear however from figures 6.2 and 6.4 that the definitions of the Brillouin threshold based on the minimum of the Brillouin linewidth and the point of inflection of the output Stokes vs. input pump curve can still be used to experimentally determine the threshold for the BFA configuration. These definitions for the threshold power in a Brillouin fiber amplifier have been defined by Ravet (2007) and verified, in part, by the experimental data presented in this chapter.

6.2 Spectral hole burning and side-lobes in stimulated Brillouin scattering

In recent years, an interesting phenomenon known as SBS spectral hole burning has been getting increasing attention (Stepien, 2002). Most of the published results so far on this topic have been concerned with cw pump and Stokes waves. In this thesis, the spectral hole burning phenomenon is observed and investigated for high power 2 ns Stokes pulses.

A comparative study was conducted using 2 ns pulses (shorter than phonon lifetime) and both narrow linewidth fiber lasers and broader linewidth DFB lasers to investigate the effects of pump power, laser linewidth, and fiber length on the development and characteristics of the central dip for narrow 2 ns pulses. The system setup used for this investigation is similar to that shown in figure 3.1, except that Erbium doped fiber amplifiers (EDFA) were inserted after the EOM to amplify the Stokes pulses to higher power as well as in the pump arm to allow for larger pump power. Injecting large pump power into the fiber along with large Stokes pulse (greater than 30 mW) results in a Brillouin loss spectrum with a "dip" in the central region at the Brillouin frequency of the fiber. An example of this dip can be seen in figure 6.6 centered on the Brillouin frequency of the fiber which was 10860 MHz.

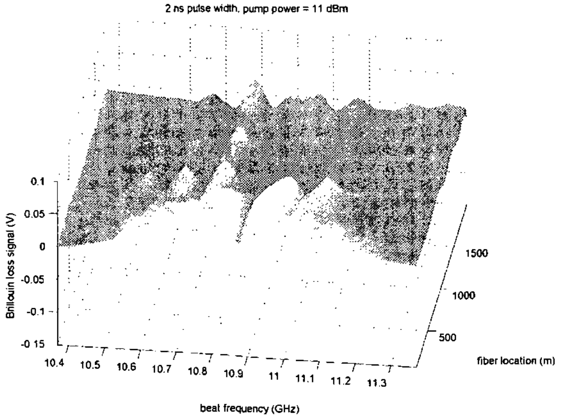

Figure 6.6 Example of central dip in Brillouin spectrum.

First a profile of the 2 ns Stokes pulse was measured and the spectrum of the pulse was determined by the Fourier transform. Figure 6.7 shows the pulse profile and reveals an unwanted small secondary pulse which follows roughly 10 ns after the main pulse. This secondary pulse is responsible for the "side lobes" on the pulse spectrum shown in figure 6.8 and the Brillouin spectrum in figures 6.6 and 6.9 through 6.13 and explains why the lobes are separated by 100 MHz (because 1/(10 ns) = 100 MHz).

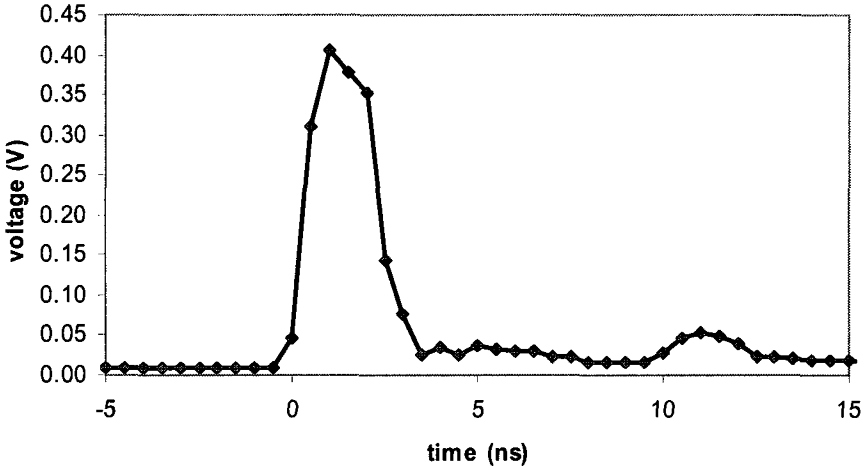

Figure 6.7 2 ns pulse profile.

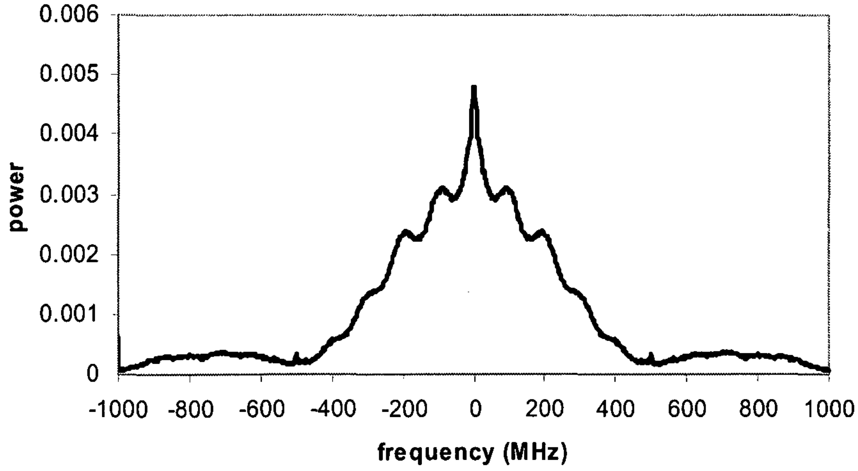

Figure 6.8 2 ns pulse spectrum calculated with FFT.

Figure 6.9 shows the results of a calculation performed by my colleague Feng Wang to determine the shape of the Brillouin spectrum that results from an input Stokes pulse with the "double pulse" characteristics of a 2 ns pulse one tenth the power of the main pulse following it by 10 ns. The calculation consisted of convoluting the spectrum of the pulse profile with the natural Lorentzian Brillouin gain spectrum. The resulting Brillouin spectral shape closely matches the shapes of the Brillouin spectra measured experimentally. This makes sense considering that the measured Brillouin spectrum can be approximated as the convolution of the natural Brillouin spectrum with the pulse spectrum.

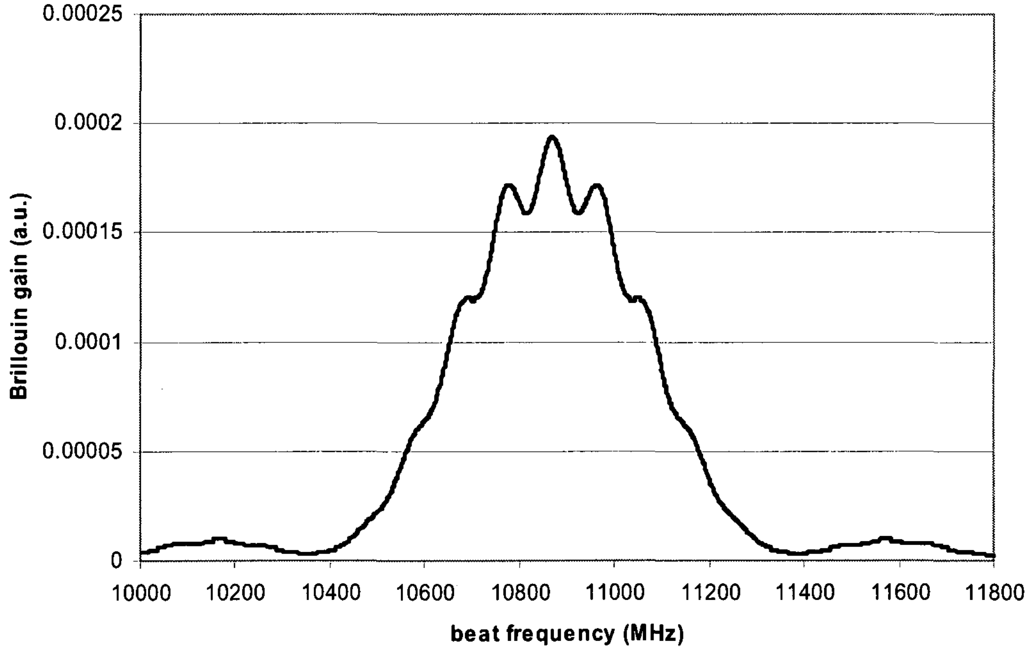

Figure 6.9 Calculated Brillouin spectrum using double pulse.

It is interesting to note that a distributed sensor system has been proposed (Koyamada, 2007) which intentionally produces modulation fringes on the Brillouin spectrum. This double-pulse BOTDA system is similar to a standard BOTDA except that a very narrow double pulse is sent down the fiber which results in a detected Brillouin spectrum that is very broad but has narrower peaks modulated on it. The claim is that cm spatial resolution can be achieved while still allowing accurate determination of the Brillouin frequency shift (4 cm spatial resolution with frequency accuracy of 1-2 MHz over a 5 km sensing fiber).

Brillouin spectra were collected in the usual way of observing the loss of the cw pump wave at different beat frequencies between the pump and Stokes lasers. Figure 6.10 shows Brillouin spectra collected from the beginning of the 2 km sensing fiber using 2 ns Stokes pulses and narrow linewidth fiber lasers, the pump power was varied from -15 dBm up to 13 dBm (0.03 mW to 20 mW). From the collected data, it is interesting to see a dip in the Brillouin spectrum whose width and depth depend on the power of the input pump wave. It appears that the dip is not present at 1.3 dBm pump power but that it does occur at both lower and higher pump powers, being particularly large and broad at very large pump power. Figure 6.11 shows a zoomed in view of the central portion of the Brillouin spectrum at 9 dBm and 15 dBm, revealing that the width of the dip increases significantly with increasing pump power.

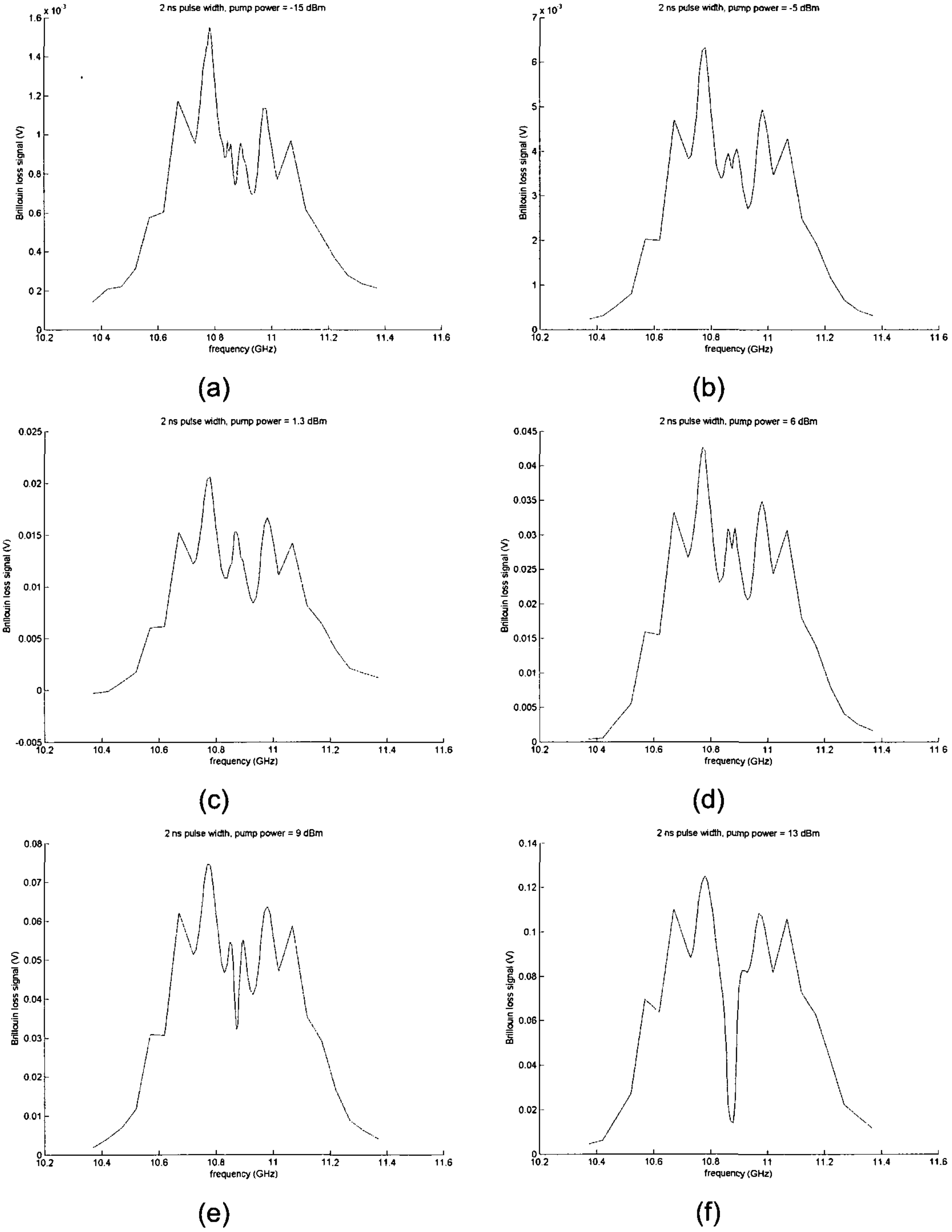

(a) (b)

(c) (d)

(e) (f)

Figure 6.10 Brillouin spectrum evolution with pump power using 2 ns Stokes pulses and narrow linewidth fiber lasers.

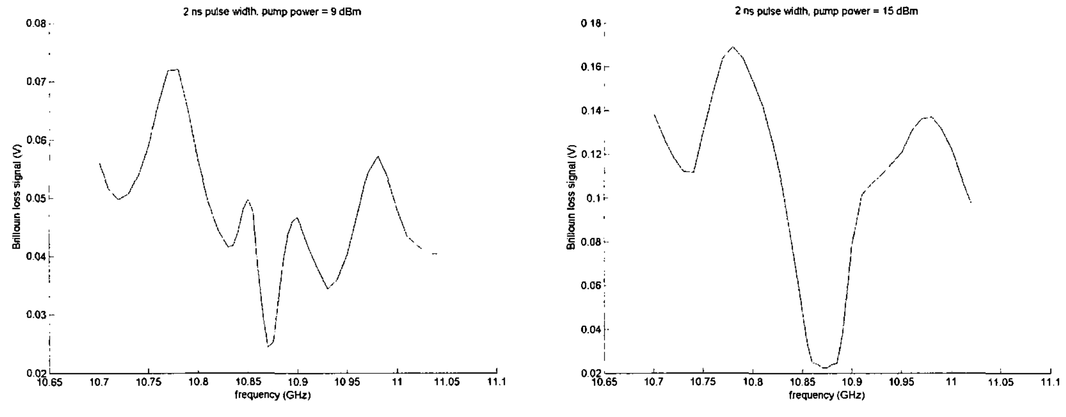

(a) (b)

Figure 6.11 Central region of Brillouin spectrum evolution with pump power using 2 ns Stokes pulses and narrow linewidth fiber lasers.

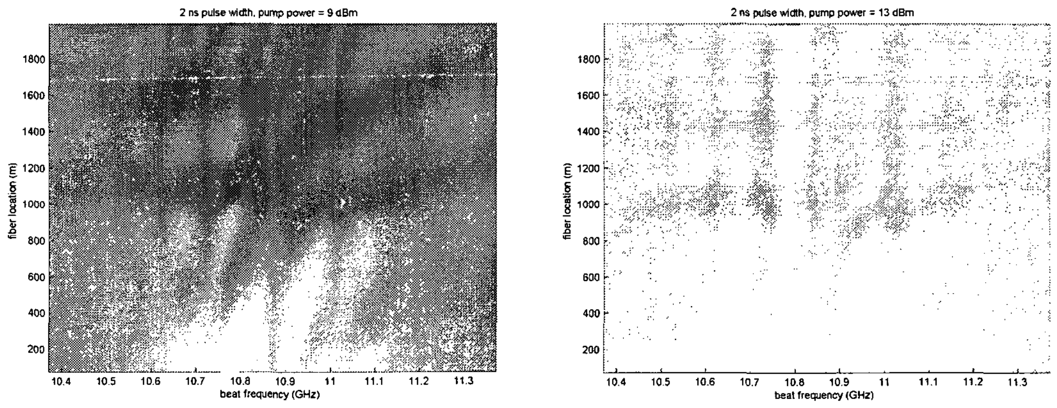

(a) (b)

Figure 6.12 Map of Brillouin loss signal over entire fiber length for (a) 9 dBm pump and (b) 13 dBm pump (lighter regions correspond to greater Brillouin loss).

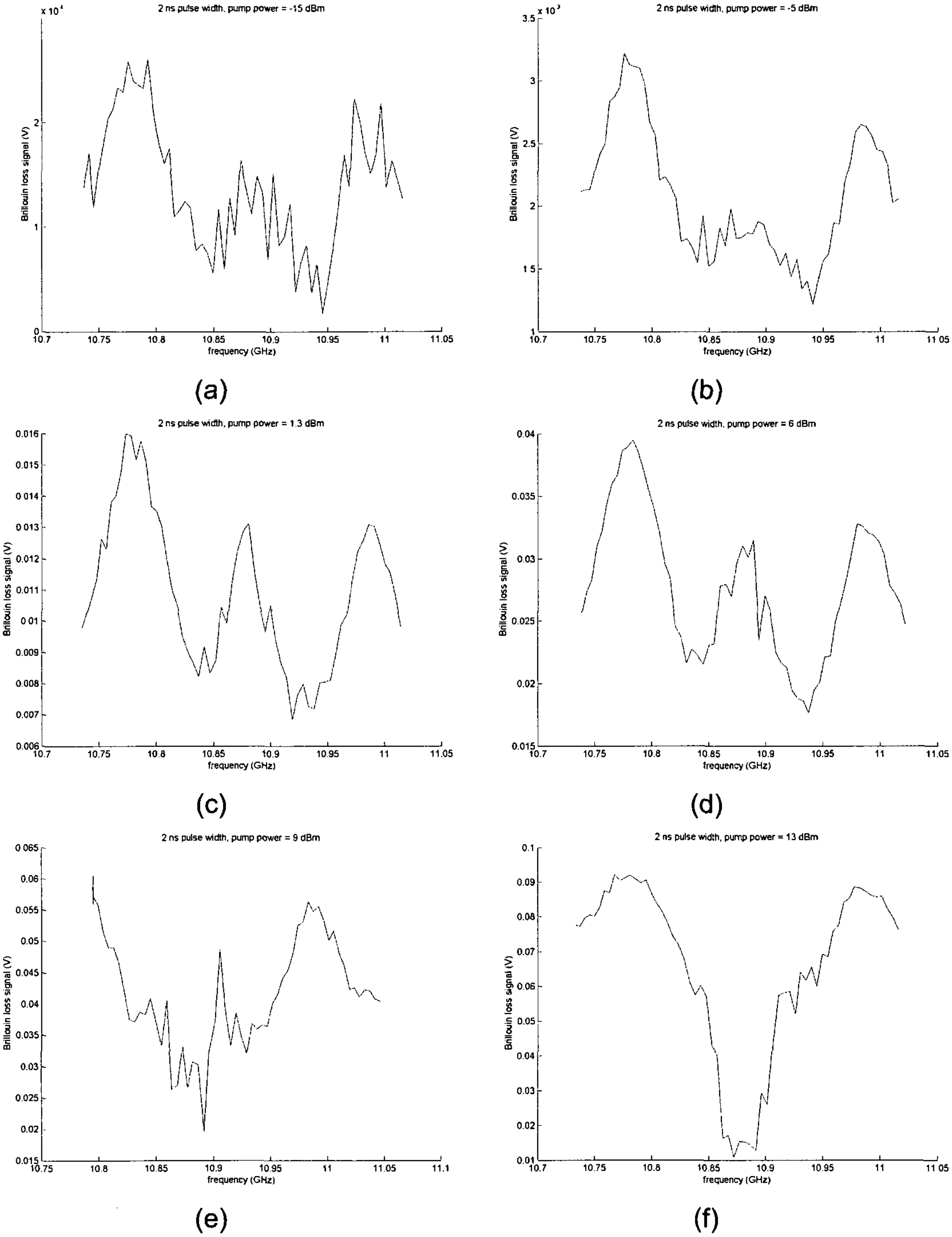

(a) (b)

(c) (d)

(e) (f)

Figure 6.13 Brillouin spectrum evolution with pump power using 2 ns Stokes pulses and broader linewidth DFB lasers.

Figure 6.12 shows a map of the Brillouin loss signal through the entire length of the 2 km fiber for (a) $P_{pump} = 9$ dBm and (b) $P_{pump} = 13$ dBm.

Figure 6.13 shows Brillouin spectra collected from the beginning of the 2 km sensing fiber using 2 ns Stokes pulses and broader 2 MHz linewidth DFB lasers. The same pattern of development of the central dip is evident when switching from the narrow linewidth fiber lasers to the larger bandwidth DFB lasers.

A better pulse generator that produces a cleaner 2 ns pulse with no secondary pulse was added to the system. The pulse profile and resulting pulse spectrum are shown in figures 6.14 and 6.15 respectively.

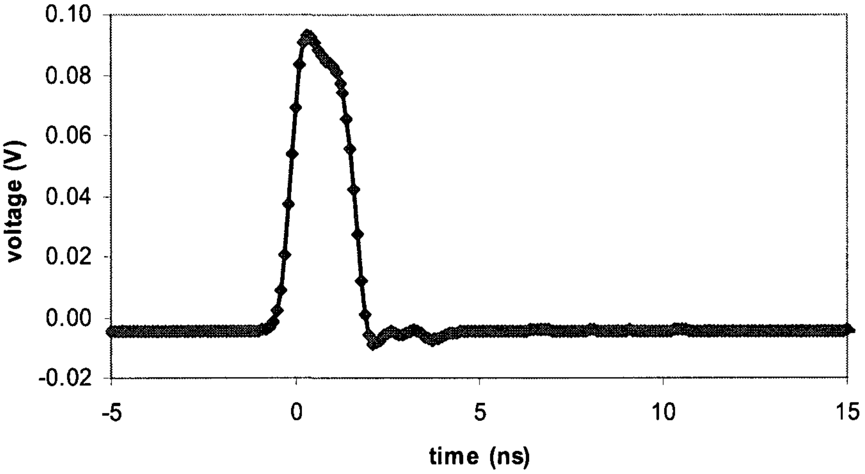

Figure 6.14 Improved 2 ns pulse profile.

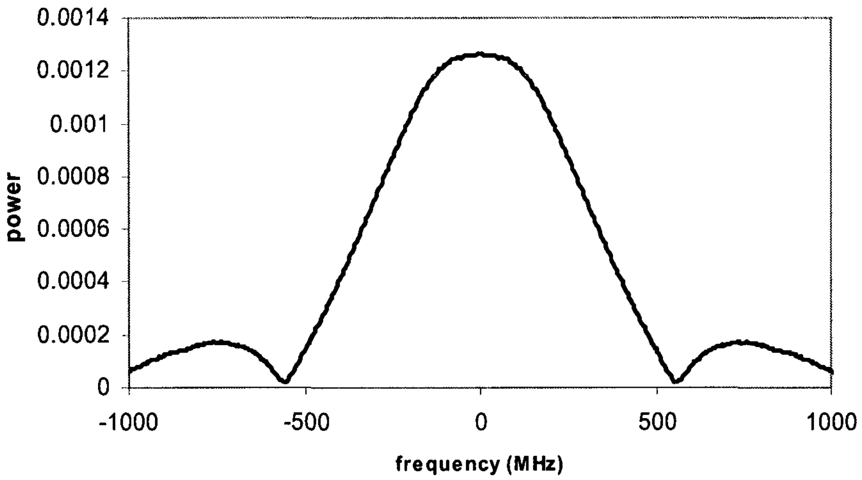

Figure 6.15 2 ns pulse spectrum calculated with FFT.

Using the improved pulse generator, an experiment was carried out by my colleague Yun Li, to try to get a better picture of the central dip without interference from the side-lobes previously caused by the poor pulse profile. Also, the effect of fiber length on the central dip was investigated. Figure 6.16(a) and (b) show the measured spectra for 2 km fibers and P_{pump} = 0 dBm and P_{pump} = 11 dBm respectively. Just as before, the central dip deepens and widens with increasing pump power. Figure 6.16(c) and (d) are for 100 m fiber with 0 and 11 dBm pump power. For the shorter fiber length, there is no evidence of the central dip.

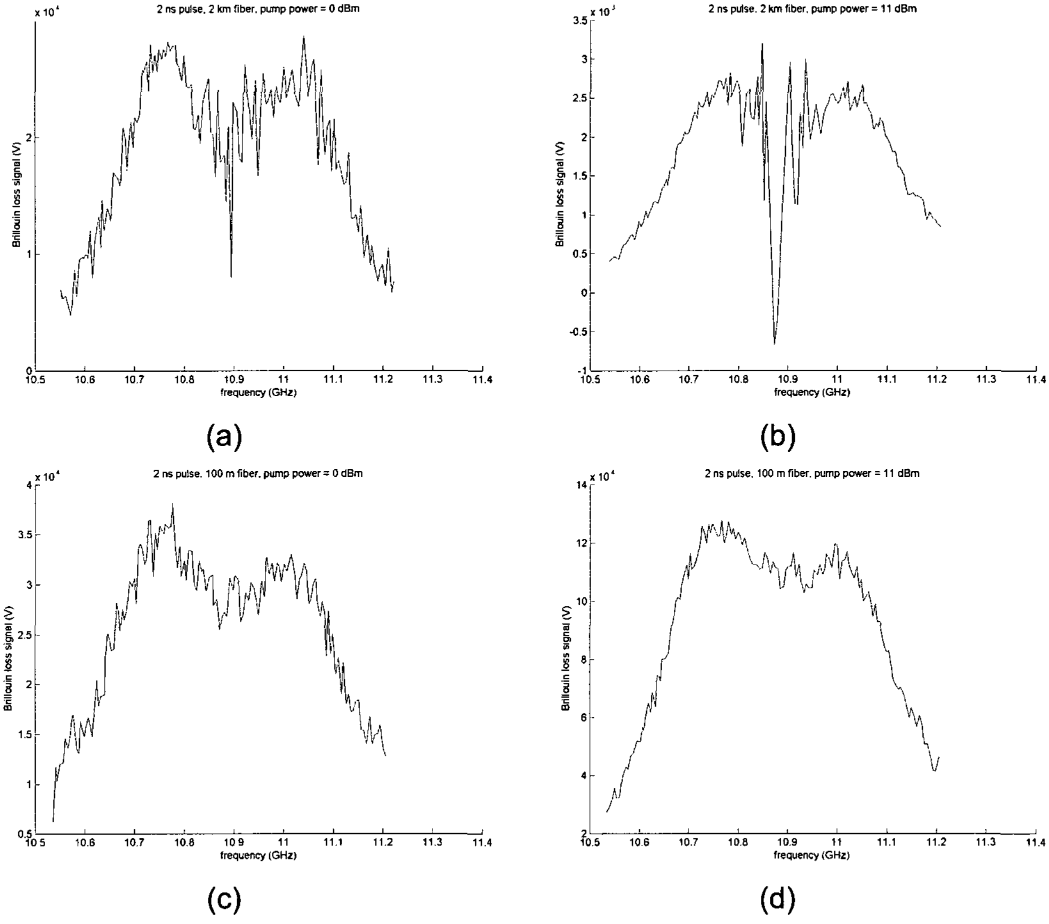

(a) (b)

(c) (d)

Figure 6.16 Brillouin spectrum using improved pulse generator, 2 ns Stokes pulses, DFB lasers, and 2 km fiber (a, b) or 100 m fiber (c, d).

From these investigations, it is clear that the side-lobes on the Brillouin spectrum are indeed caused by the presence of the secondary pulse which followed roughly 10 ns after the main pulse. The Brillouin spectra measured with the cleaner input pulse show no side lobes. Also, it has been determined that the laser linewidth of the pump and Stokes lasers do not play an important role in the characteristics of the central dip. Both the narrow linewidth fiber lasers and the broader linewidth DFB lasers show similar evolution of the central dip with pump power.

An explanation of the behaviour of the central portion of the Brillouin spectrum is as follows. At low pump power there is a small dip in the center of the Brillouin spectrum which disappears and eventually raises into a peak as the pump power is increased (visible in the 1.3 dBm plot). This raising of the central component is due to Brillouin scattering of the Stokes pulse. When the very large power Stokes pulse of frequency ν_0 - ν_B travels down the fiber, a significant amount of power is spontaneously Brillouin backscattered and travels in the same direction as the pump wave (figure 6.17). The Stokes component of this scattering of the pulse occurs at a frequency of ν_0-$2\nu_B$ and so is not present in the spectra being recorded. However, the Stokes pulse anti-Stokes component (S.A.S.) is at a frequency of ν_0, the same frequency as the input pump wave and shows up in the measured spectra as an increase in pump power, thus decrease in pump loss, which explains the dip in the Brillouin loss spectrum at low pump power. As the pump power is increased, the Brillouin interaction between the pump and Stokes pulse strengthens resulting in greater Brillouin loss of the pump wave, however, the power of the S.A.S. component remains unchanged and thus the dip gradually disappears.

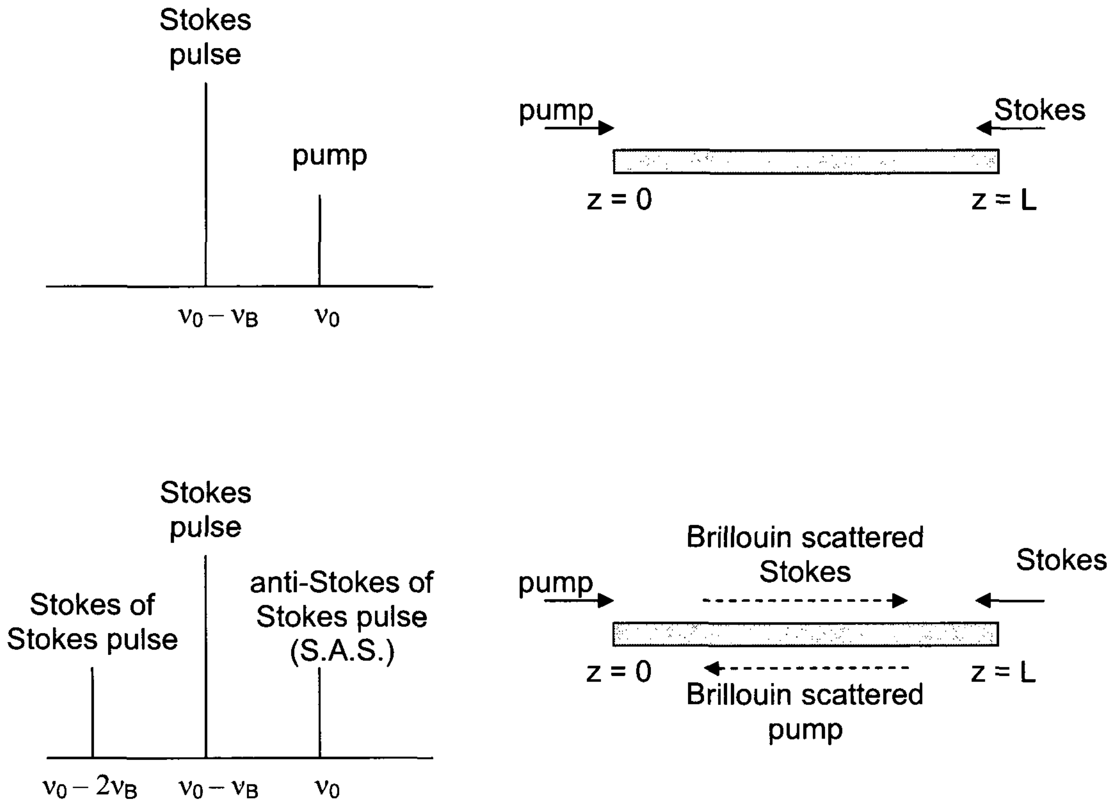

Figure 6.17 Brillouin scattering of Stokes pulse.

As the power of the pump injected into the fiber is increased, the amplitude of the acoustic field continues to increase, scattering light from the pump wave to the counter-propagating Stokes wave. At a certain point, the acoustic field associated with the center of the Brillouin spectrum is saturated and cannot increase in amplitude any further because the pump power is being depleted at that frequency. At this point, pump power is no longer able to be efficiently scattered to the Stokes field downshifted by the Brillouin frequency. Instead, the pump power is more efficiently scattered into the Stokes waves at frequencies which are detuned from the central frequency. This results in the central frequency of the Brillouin loss spectrum developing a dip. At very high pump power, the gain becomes saturated even for frequencies detuned from the Brillouin frequency of the fiber, resulting in a broadening of the dip which is particularly evident when comparing figures 6.11(a) and (b) to see how the dip evolves from $P_{pump} = 9$ dBm to $P_{pump} = 15$ dBm.

The phenomena of the side lobes on the Brillouin spectrum and the dip at the center of the Brillouin spectrum have been observed and explained. While, the side lobes caused by double Stokes pulses have been documented for the case of pulses of equal power (Koyamada, 2007), it is important to realize that a similar modulation of the Brillouin spectrum can occur when a secondary pulse of much lower power is injected into the fiber, such as can occur with a faulty pulse generator. The phenomenon of spectral hole burning in the detected Brillouin spectrum is one that is important for sensing applications as it is important to avoid changes from a simple Lorentzian or Gaussian spectral profile for peak-fitting purposes. Low pump power with high Stokes pulse power should be avoided so that the dip in the spectrum from Brillouin scattering of the Stokes pulse does not occur. Also, high pump power should be avoided so that gain saturation and its associated spectral dip does not occur.

Chapter 7

Conclusion

7.1 Thesis outcomes

In distributed Brillouin sensors, the characteristics of the pulse are very important to sensing performance. Two different methods of locking the pulse base level have been examined and have found to both have applications in which they excel. The PID control method is ideal when a certain DC level is desired (for example to reduce the Brillouin linewidth when using pulses of short duration). The lock-in amplifier method is ideal when the pulse base is to be kept as low as possible with the highest possible extinction ratio, however, this method is not effective when the pulse base is to be locked to any value other than the maximum extinction ratio. Also, the PID method was extended to locking the pulse base, top, and duration simultaneously and has functioned admirably.

A feasibility study on the use of the stimulated Brillouin scattering effect in vibration sensing has been conducted. It has been found that the technique has promise, showing a 2 m spatial resolution in a 100 m fiber and 50 Hz acquisition rate in the lab, as well as the ability to detect vehicles as they pass quickly over a concrete highway. However, this technique does not allow the measurement of the full Brillouin spectrum of the fiber under test and thus does not yield the actual strain or temperature – just the frequency of vibration and timing of events. This sensor in its present configuration also has issues with unequal sensitivity throughout various regions of the sensing fiber.

The threshold definitions given by Ravet (2007) for the Brillouin fiber amplifier configuration has been verified as a useful definition of the Brillouin threshold in place of previous definitions which were not capable of taking the input Stokes power into account. These definitions are: i) the power at which the Brillouin linewidth reaches a minimum, and ii) the power at which there is a point of inflection in the logarithmic plot of output Stokes power vs. input pump power.

Finally, an interesting phenomenon of spectral hole burning in stimulated Brillouin scattering has been investigated for high power 2 ns Stokes pulses. The central portion of the Brillouin spectrum has been observed to first grow as the pump power is increased and then to reverse its growth and develop a dip as the pump power is further increased. This behaviour is explained as being caused first by the Brillouin scattering of the high power Stokes pulse and then by the saturation of the gain at the Brillouin frequency for higher pump power.

7.2 Future work

Since it would be beneficial to have the option of locking the pulse base level using a different method based on the sensing conditions, a system should be developed for the distributed Brillouin sensor which would allow either method to be selected by the user.

The studies presented in chapter 5 of this thesis concerning a vibration sensor based on stimulated Brillouin scattering are a proof-of-concept only and further work needs to be done to develop the system into a viable real-time vibration sensor. Among the required work, most important would be implementation and thorough field testing of the sensor in an application such as monitoring the response of a bridge to the passage of heavy vehicles. Also, sensitivity improvements due to alternative detection schemes such as polarization dependent detection should be investigated.

A systematic study of the occurrence of the central dip at high Stokes pulse power and low cw pump power should be completed. The effect of Stokes power, pump power, fiber length, and pulse duration should be thoroughly investigated so that the occurrence of the central dip can be avoided during sensing operation.

References

G.P. Agrawal, *Nonlinear Fiber Optics 3rd edition*, 2001 Academic Press, San Diego.

K. Astrom and T. Hagglund, *PID Controllers: Theory, Design, and Tuning 2nd Ed.* (Instrument Society of America, 1995).

X. Bao, D. J. Webb, D. A. Jackson, "22 km distributed strain sensor using Brillouin loss in an optical fiber," Optics Communications **104,** 298–302 (1994).

X. Bao, J. Dhliwayo, N. Heron, D. J. Webb, D. A. Jackson, "Experimental and Theoretical Studies on a Distributed Temperature Sensor Based on Brillouin Scattering," J. Lightwave Technol. **13,** 1340-1348 (1995).

X. Bao, D. J. Webb, D. A. Jackson, "Distributed temperature sensor based on Brillouin loss in an optical fiber for transient threshold monitoring," Canadian Journal of Physics **74,** 1-3 (1996).

X. Bao, A. Brown, M. DeMerchant, and J. Smith, "Characterization of the Brillouin-loss spectrum of single-mode fibers by use of very short (<10-ns) pulses," Opt. Lett, vol 24, 510-512 (1999).

X. Bao, M. DeMerchant, A. Brown, T. Bremner, "Tensile and compressive strain measurement in the lab and field with the distributed Brillouin scattering sensor," J. Lightwave Technol. **19**, 1698-1703 (2001).

X. Bao, Q. Yu, V. P. Kalosha, L. Chen, "Influence of transient phonon relaxation on the Brillouin loss spectrum of nanosecond pulses," Opt. Lett. **31**, 888-890 (2006).

R.W. Boyd, *Nonlinear Optics 2nd Edition*, 2003, Academic Press.

F. Chang, Structural Health Monitoring: from diagnostics & prognostics to structural health management (DEStech, 2003).

R. Y. Chiao, C. H. Townes, B. P. Stoicheff, "Stimulated Brillouin scattering and coherent generation of intense hypersonic waves," Phys. Rev. Lett. **12**, 592-595 (1964).

D. Culverhouse, F. Frahi, C. N. Pannell, D. A. Jackson, "Potential of stimulated Brillouin scattering as sensing mechanism for distributed temperature sensor," Electron. Lett. **25**, 913-914 (1989).

M. O. V. Deventer, A. J. Boot, "Polarization properties of stimulated Brillouin scattering in single-mode fibers," J. Lightwave Technol. **12**, 585-590 (1994).

I. L. Fabelinskii, *Molecular light scattering*, 1968, Plenum Press, New York.

G. A. Ferrier, X. Bao, L. Zou, L. Chen, "Distributed Brillouin temperature measurements without frequency scanning for dynamic process monitoring," Proc. of SPIE **5393,** 66-75 (2004).

E. Gross, "Change of wave-length of light due to elastic heat waves at scattering in liquids," Nature **126**, 201-202 (1930).

T. Horiguchi, T. Kurashima, M. Tateda, Y. Koyamada, "Tensile strain of Brillouin frequency shift in silica optical fibers," IEEE Photo. Tech. Lett. **1**, 107-109 (1989).

T. Horiguchi, K. Shimizu, T. Kurashima, M. Tateda, Y. Koyamada, "Development of a distributed sensing technique using Brillouin scattering," J. Lightwave Technol. **13**, 1296-1302 (1995).

K. Hotate, S. S. L. Ong, "Distributed dynamic strain measurement using a correlation-based Brillouin sensing system," IEEE Photonics Technol. Lett. **15**, 272-274 (2003).

D. A. Humphreys, "Integrated-optic system for high-speed photodetector bandwidth measurements," Electron. Lett. **25,** 1555-1557 (1989).

R. L. Jungerman, C. Johnsen, D. J. McQuate, K. Salomaa, M. P. Zurakowski, R. C. Bray, G. Conrad, D. Cropper, P. Hernday, "High-Speed Optical Modulator for Application in Instrumentation," J. Lightwave Technol. **8,** 1363-1370 (1990).

Y. Koyamada, "Proposal and simulation of double-pulse Brillouin optical time-domain analysis for measuring distributed strain and temperature with cm spatial resolution in km-long fiber," IEICE Trans. Commun. **90**, 1810-1815 (2007).

T. Kurashima, T. Horiguchi, and M. Tateda, "Distributed-temperature sensing using stimulated Brillouin scattering in optical silica fibers," Optics Letters **15,** 1038-1040 (1990).

T. Kurashima, T. Horiguchi, and M. Tateda, "Thermal effects on the Brillouin frequency shift in jacketed optical silica fibers," Appl. Opt. **29,** 2219 (1990).

V. Lecoeuche, D. J. Webb, C. N. Pannell, and D. A. Jackson, "Transient response in high-resolution Brillouin-based distributed sensing using probe pulses shorter than the acoustic relaxation time," Opt. Lett. **25,** 156-158 (1999).

G. L. Li and P. K. L. Yu, "Optical Intensity Modulators for Digital and Analog Applications," J. Lightwave Technol. **21,** 2010-2030 (2003).

Y. Li, X. Bao, J. Snoddy, L. Chen, "Brillouin spectrum narrowing in high extinction ratio nanosecond pulse from phase locked DFB lasers," submitted to J. Lightwave Technol. (2008).

M. L. Meade, *Lock-in amplifiers: principles and applications* (Peter Peregrinus Ltd, 1983).

H. Naruse, M. Tateda, "Trade-off between the spatial and the frequency resolutions in measuring the power spectrum of the Brillouin backscattered light in an optical fiber," Appl. Opt. **38,** 6516-6521 (1999).

NP Photonics, *Scorpion Benchtop Erbium Micro Fiber Laser: Operating instructions & user manual Version 3.2.* (2006).

S. C. Rashleigh, "Origins and control of polarization effects in single-mode fibers," J. Lightwave Technol. **LT-1**, 312-331 (1983).

F. Ravet, 2007. PhD Thesis, University of Ottawa.

V. Shahraam Afshar, G. A. Ferrier, X. Bao, and L. Chen, "Effect of the finite extinction ratio of an electro-optic modulator on the performance of distributed probe-pump Brillouin sensor systems," Opt. Lett. **28,** 1418-1420 (2003).

J. Smith, A. Brown, M. DeMerchant, X. Bao, "Pulse width dependence of the Brillouin loss spectrum," Opt. Comm. **168**, 393-398 (1999).

R. G. Smith, "Optical power handling capacity of low loss optical fibers as determined by stimulated Raman and Brillouin scattering," Applied Optics **11**, 2489-2494 (1972).

K. Song, K. Hotate, "Enlargement of measurement range in a Brillouin optical correlation domain analysis system using double lock-in amplifiers and a single-sideband modulator," IEEE Photonics Technol. Lett. **18**, 499-501 (2006).

J. M. Stallings, J. W. Tedesco, M. El-Mihilmy, M. McCauley, "Field performance of FRP bridge repairs," Journal of Bridge Engineering **5**, 107-113 (2000).

L. Stepien, S. Randoux, J. Zemmouri, "Origin of spectral hole burning in Brillouin fiber amplifiers and generators," Phys. Rev. A **65**, 053812 1-13 (2002).

R. Tennyson, "Installation, Use and Repair of Fibre Optic Sensors" ISIS Canada Corp., Winnipeg, Manitoba (2001).

A. Villafranca and J.A. Lazaro, "Stimulated Brillouin scattering gain profile characterization by interaction between two narrow-linewidth optical sources," Optics Express **13**, 7336-7341 (2005).

D. Waddy, P. Lu, L. Chen, X. Bao, "Fast state of polarization changes in aerial fiber under different climatic conditions," IEEE Photonics Technol. Lett. **13**, 1035-1037 (2001).

XL Microwave Inc., Models 3201 & 3261 Operating and Maintenance Manual.

A. Yeniay, J. Delavaux, J. Toulouse, "Spontaneous and stimulated Brillouin scattering gain spectra in optical fibers," J. Lightwave Technol. **20,** 1425-1432 (2002).

L. Zou, X. Bao, Y. Wan, L. Chen, "Coherent probe-pump-based Brillouin sensor for centimeter-crack detection," Opt. Lett. **30,** 370-372 (2005).

Publications

J. Snoddy, Y. Li, F. Ravet, and X. Bao, "Stabilization of electro-optic modulator bias voltage drift using a lock-in amplifier and a proportional-integral-derivative controller in a distributed Brillouin sensor system," Appl. Opt. **46**, 1482-1485 (2007).

F. Ravet, J. Snoddy, X. Bao, and L. Chen, "Power thresholds and pump depletion in Brillouin fiber amplifiers," The Open Optics Journal, **2,** 1-5 (2008).

S. Yang, J. Cameron, J. Snoddy, L. Zou, and X. Bao, "PRBS data delay in an all fiber slow light system based on SBS effect, NRZ vs. RZ," IEEE OFC/NFOEC, 1-26 (2007).

Update and revision of ISIS Canada Design Manual No.1:

R. Tennyson, "Installation, Use and Repair of Fibre Optic Sensors" ISIS Canada Corp., Winnipeg, Manitoba (2001).